Final Technical Report for
Nuclear Regulatory Commission Job Code N6501 Task 4

Aleatory and epistemic uncertainties in interpolated ground motions – Example from the Kashiwazaki-Kariwa Nuclear Power Plant recordings of the July 16, 2007, Niigata-ken Chuetsu-oki, Japan, earthquake

Paul Spudich[1]
Antonella Cirella[2]

11 October 2011

[1] U.S. Geological Survey
345 Middlefield Road
Menlo Park, CA 94025 USA
+1-650-329-5654
spudich@usgs.gov
(Corresponding Author)

[2] Istituto Nazionale di Geofisica e Vulcanologia
Via di Vigna Murata, 605
00143 Roma, ITALY
+39 0651860545
antonella.cirella@ingv.it

This page deliberately left blank.

Aleatory and epistemic uncertainties in interpolated ground motions – Example from the Kashiwazaki-Kariwa Nuclear Power Plant recordings of the July 16, 2007, Niigata-ken Chuetsu-oki, Japan, earthquake

Paul Spudich[1]
Antonella Cirella[2]

[1] U.S. Geological Survey
345 Middlefield Road
Menlo Park, CA 94025 USA
+1-650-329-5654
spudich@usgs.gov
(Corresponding Author)

[2] Istituto Nazionale di Geofisica e Vulcanologia
Via di Vigna Murata, 605
00143 Roma, ITALY
+39 0651860545
antonella.cirella@ingv.it

Administrative Report

U.S. Department of Interior

U.S. Geological Survey

U.S. Department of the Interior

Ken Salazar, Secretary

U.S. Geological Survey
Marcia K. McNutt, Director

U.S. Geological Survey, Reston, Virginia: October 2011

Abstract

We quantify the scatter of absolute spectral acceleration, SA, predicted at Kashiwazaki-Kariwa Nuclear Power Plant (KKNPP) based on rupture models derived from waveform inversion of a set of Niigata-area accelerograms from the July 16, 2007, Chuetsu, Japan, earthquake. In an initial inversion we obtain a set of thousands of 'good' kinematic rupture models which we use to predict SA at the KKNPP. The scatter in the predicted horizontal response spectra at KKNPP from the inversion is about 22% bigger than the scatter of response spectra predicted at the Niigata stations. We relate the scatter in the predicted motion to the spatial isolation of the prediction site. We compare our scatter with aleatory variation of ground motions from kinematic and dynamic rupture models. Almost all of the aleatory scatter values of the ground motions from kinematic rupture models exceed the empirically observed scatter in response spectra from a standard ground motion prediction equation. The aleatory variation of dynamic rupture ground motions is much smaller than that of the kinematic rupture models, indicating that the correlations of dynamic models' source properties cause lower ground motion variability. The aleatory variability of dynamic rupture ground motion is comparable to the empirically observed variability. Our scatter at KKNPP approaches the empirically observed interevent scatter. This means that the variability of predicted motion at KKNPP from the nonuniqueness of the rupture inversion is almost as great as the variability of motion incurred by using a different earthquake having the same magnitude and hypocenter to predict the motion.

This page intentionally left blank.

Introduction

When earthquakes occur, seismologists are usually in the predicament of having a few recordings of ground motion, but not at sites where something interesting and/or bad occurred, such as building damage. Consequently, in post-earthquake forensic studies seismologists are usually called upon to estimate the unobserved ground motions at the site of the damage. Recently, seismologists have developed systems to produce maps of ground shaking within a few minutes of the occurrence of an earthquake. Such maps merge observations of ground motions at (usually) small numbers of sites (10–50) with some sort of model of earthquake shaking which is used to estimate ground motions everywhere between the observation locations. Both the post-earthquake forensic studies and the 'shake-map' generation rely upon ground-motion interpolation, which is the process of inferring, from a set of observed ground motions from a single earthquake, the ground motions that would have been recorded at a target site where no observations were made during the earthquake.

In general the ground-motion interpolation process requires that some sort of assumed interpolating function be fitted to the observations and evaluated at the target site. For simple processes such as the generation of shake-maps, the interpolating function is typically a simple algebraic equation which produces a response spectral acceleration value given the earthquake's magnitude, distance from the site, and soil conditions at the site. However, it is now possible to invert observed ground motions (typically ground-velocity time series) to obtain the spatio-temporal behavior of rupture on the causative fault (that is, a rupture model). This inferred rupture model can then be used, along with wave-propagation computer codes, to calculate the ground-motion time series at the unobserved target site.

The problem with using an inverted rupture model to calculate ground motions at target sites is that many different rupture models can fit the observed data well, each of which predicts a different ground motion at the target site. For example, Cirella et al. (2008)

generated more than 18,000 different rupture models for the July 16, 2007, Chuetsu-oki, Japan, earthquake that fit the observed ground motions well (we will quantify 'well' below). If the 18,000 rupture models are used to predict the ground motions at an unobserved target site, how large is the scatter in the predicted motions (where by 'scatter' in this paper we mean the standard deviation of the predicted ground motions due to the variability of rupture models in a particular ensemble)? Is the scatter of the predicted motions large enough to include the true motions at the target site? Is the scatter of the predicted motions at the unobserved target site larger than the scatter of the predicted motions at sites having data used in the inversion?

In this paper we describe work that builds on the foundation laid by Cirella et al. (2008), who derived their rupture models for the Chuetsu earthquake from ground motions recorded on 13 Niigata-region KiK-net and K-NET accelerograph stations and 14 GPS coseismic surface displacements within a 70 km epicentral distance (for brevity below we call this set of accelerograph and GPS data the 'Niigata data', Figure 1). The main difference between our work and Cirella's is that we have obtained the Chuetsu main-shock ground motions recorded at the Kashiwazaki-Kariwa Nuclear Power Plant (KKNPP) (TEPCO, undated). (In the following we refer to these ground motions as the 'KK data.') Thus, we can 'predict' the motions at the KKNPP and compare them to the actual observed motions. KKNPP data were chosen to study because this earthquake damaged the KKNPP, so the question of the predictability of ground motions at the plant is especially interesting.

Theoretically, the process of ground-motion interpolation as described above is an example of linear inference (for example, Parker, 1994, section 4.0.3). For a linear problem lacking bounds on the model space, under some circumstances (discussed later), the interpolated ground motion can be completely unconstrained by the data. When bounds like positivity and known moment are added as constraints on the model, the interpolated motions may then become bounded. Algorithm BVLS of Stark and Parker (1995) can compute bounds on linear functionals of an inverted model. However, the response spectrum is a nonlinear function of the ground acceleration time series, and

consequently we have chosen to investigate the variability of interpolated response spectra using a statistical approach building on Cirella's work.

We ask the following questions:

1. If we invert the Niigata data set (without the KK data) and we predict the KK motions from the ensemble of thousands of 'good' rupture models, what is the mean bias of the predicted motions (that is, observed minus predicted log spectral accelerations), and what is the scatter of the predicted motions?

2. How do the scatters of the calculated motions at KK from the inversion omitting and including the KK data compare to each other?

3. How does the scatter of the predicted motions at KK (from the inversion omitting the KK data) compare to the average scatter of motions at the Niigata stations?

4. Can we identify factors that affect the scatter of predicted motions at KK?

5. How does the scatter of the predictions at KK compare to published estimates of aleatory variability in kinematic and dynamic rupture models?

Data and Environment

The KKNPP was extensively instrumented before the earthquake (TEPCO, undated), and although many instruments failed to record the main shock, a useful number of main-shock recordings were made. Figure 2 shows the locations of stations 1g1, 5g1, and sg1, the ground-level free-field accelerometers that recorded the main shock. Instrument characteristics are given in TEPCO (undated).

Site conditions at 1g1 and 5g1 can be inferred from boreholes logged near them (Figure 2), specifically, boreholes containing accelerometers g07-g10 near 1g1, and g51-g55

near 5g1. Station sg1 was emplaced at 2.4 m depth in a logged borehole. Shear velocity profiles are shown in Figure 3 for these three boreholes. Table 1 gives a geologic profile of the three boreholes, simplified from TEPCO (undated).

Figure 4 shows the integrated accelerograms (high pass filtered at 0.1 Hz with an acausal Butterworth filter). Note that ground motions are very similar at 1g1 and 5g1, but that ground motions at sg1 are largely depleted of high frequencies. We interpreted this lack of high frequencies to indicate significant nonlinear soil response at sg1, which is not surprising given its 70 m layer of sand, so we omitted this station's data from subsequent analysis. We assumed linear soil response in the analysis of 1g1 and 5g1 data.

The 'Niigata' accelerographs consisted of KiKnet stations (stations having an 'H' in their name, Figure 3) and K-net stations (the remaining stations). Each KiKnet station had a near-surface and a downhole accelerometer at 100 – 200 m depth; in this study we used the downhole sensors to avoid site effects. Unfiltered motions downhole are considerably smaller than at the surface, but at periods greater than 2 s, the period band of our analysis, the near-surface and borehole stations' velocity time series are nearly identical, so we can approximate that the selected sensors are at the surface. This implies that site effects in our period band are minimal, at least at the KiKnet stations. We excluded some data recorded near KKNPP from consideration. We excluded data from GPS benchmarks 960566 and 960567, because the instrumentation and/or the corrected coseismic displacements might have problems, and data from accelerograph NIG018, which is strongly affected by nonlinear site effects (S. Aoi, personal communication, 2008 and K. Koketsu, personal communication, 2008). However, we have verified that including or excluding these data does not affect the inverted rupture model.

Development of a 1D Velocity Structure at KKNPP

Because our ground motion prediction method requires a 1D velocity structure, we develop such a structure based on geologic information from the KKNPP site. Shallow P- and S-wave velocities are available (TEPCO, undated) to depths of about 300 m from logged boreholes containing sensors g07-g10, g51-g55, and sg1-sg4 (Figure 2 and Figure 3). Deeper P- and S-wave velocities were taken from a 1D profile beneath point K1 in a two-dimensional (2D) structure derived from seismic reflection information and deep oil company boreholes (TEPCO, 2008, p. 31; Watanabe et al., 2011). Deepest velocities were from the structure used by Cirella et al. (2008). All these profiles are shown in Figure 3, along with our inferred 1D gradient nonattenuating structure TG3 (Table 2) which we used for subsequent ground-motion modelling at the KKNPP. Formation densities were derived from seismic velocities using relations from Brocher (2005). We do not model 1D site effects explicitly; our 1D structure TG3 is a good average of the shallow borehole velocity structures (Figure 3) but does not agree exactly with any specific borehole profile. The main site effects are probably caused by the 2D or 3D geologic structure under the KKNPP. As we discuss in more detail later, an unmodeled site effect will not affect our estimation of the scatter of predicted motions at KKNPP.

Simulation of Aftershock Ground Motions

In order to determine the likely ground motion errors to be incurred by using structure TG3, we used the known point source mechanisms of several moderate-sized aftershocks to forward-predict ground motions at KKNPP, which we then compared to the aftershock data recorded at the KKNPP (Table 3, Figure 1). These comparisons were done at periods sufficiently long that no rupture details were needed. We simulated the M 4.4 and 4.7 events at 1g1 as point moment tensor sources using the Japanese F-net Broadband Seismograph Network mechanisms (see Data and Resources Section) and using COMPSYN (Spudich and Xu, 2003). We were unable to simulate the M 3.2 and 3.7 events as they lacked mechanisms; the M 3.5 event ground motions were too noisy

for a meaningful comparison, and the M 5.6 was too large to be approximated by a point source.

In general the synthetic aftershock velocities are about half the amplitude of the observed motions at 1g1 (Figure 5). This amplitude discrepancy also occurs at 5g1 (not shown). Work by Watanabe et al. (2011) and work summarized in TEPCO (2008) attribute the high amplitudes at 1g1 to be caused by focussing of upcoming waves by shallow folded underground layers at KKNPP. In addition, the observations show a ringing character not seen in the simulations, possibly related to a resonance with an unknown geological heterogeneity near the site. The inaccuracies in the Greens functions obviously alias into errors in the inverted main shock rupture models and the ground motions predicted therefrom. However, we neither derived a correction factor nor did we alter the TG3 velocity structure to fix these problems because we are trying to see how well motions could have been predicted at the KKNPP based on velocity-structure information knowable in principle before the main shock.

Inversions for Main-Shock Rupture Model Ensembles

In this work we performed three joint inversions of strong motion and GPS data by using the method of Piatanesi et al. (2007), which was also used by Cirella et al. (2008). A crucial attribute of Piatanesi's method is that, given a set of observed earthquake ground-velocity seismograms and GPS measurements, the technique uses a heat-bath simulated annealing algorithm to explore the model space extensively and to generate an ensemble of millions of rupture models that efficiently sample the good data-fitting regions of model space. The algorithm allows us to select thousands of rupture models having a cost function value smaller than a given threshold, which fit the observed motions well according to a specific cost function (misfit metric). To quantify the misfit of a model, Piatanesi et al. (2007) chose a total cost function consisting of a weighted sum of the cost functions associated with the strong motion and GPS data.

The cost function associated with the strong motion data is a frequency domain version of a cost function that was first presented by Spudich and Miller (1990). We present the time-domain version of the cost function as it is much easier to understand than the frequency-domain version. Given the *i*-th observed data seismogram $d_i(t)$ and corresponding synthetic seismogram $s_i(\mathbf{m}_j, t)$ from the *j*-th rupture model $\mathbf{m}_j$, Spudich and Miller (1990) defined the normalized misfit to be

$$M_{ij} = \int \left(d_i - s_i(\mathbf{m}_j, t)\right)^2 dt \Big/ \left(\int d_i^2 dt + \int s_i^2(\mathbf{m}_j) dt\right)$$

This misfit takes on the value 1 for uncorrelated seismograms and the value 2 (not $\sqrt{2}$ as stated in Spudich and Miller; ironically, they defined the misfit function M_{ij} but actually used $\sqrt{M_{ij}}$ in their calculations) for anticorrelated seismograms. Note that the normalization in the denominator makes this cost function less sensitive to amplitude discrepancies than an L2-norm cost function. Because absolute amplitudes are important to engineers, it might be argued that an L2 norm might be more appropriate for ground motion interpolation studies. We later show that our cost function is moderately sensitive to amplitudes and that our estimates of scatter in predicted ground motions are not strongly biased by amplitude discrepancies. Furthermore, while older inversions following the contrained linear inversion method of Olson and Apsel (1982) used the L2 norm, some modern statistical inversions use either a mixture of L1, L2, and waveform fit criteria like ours (e.g. Ji et al., 2002) or they use our criterion (Liu et al., 2006).

The misfit of the i^{th} geodetic datum is

$$G_i = \left(\frac{g_i^r - g_i^s}{\sigma_i}\right)^2 \Big/ \sum_{i=1}^{n_g} (g_i^r)^2$$

where g_i^r and g_i^s, are the i^{th} recorded and synthetic displacements, σ_i is the error of the i^{th} datum, and n_g is the number of data (Hudnut et al., 1996). Piatanesi's (and our) cost function is equivalent to

$$C(\mathbf{m}_j) = \frac{\sum_{i=1}^{n} w_i M_{ij}}{n} + \sum_{i=1}^{n_g} G_i \,/ n_g$$

where the weight w_i is 0.5 for vertical and 1.0 for horizontal component seismograms, and n is the total number of seismograms. We will call the first term on the right side of the above equation the 'seismic cost' and the second term the 'geodetic cost.'

In our inversions the typical cost of the initial rupture models was about 1.2 to 1.4. After approximately 1.5 million models had been explored, the iteration was stopped when the cost function had declined to a rough plateau level where the normalized cost was about 0.7 - 0.8, with the global minimum cost model, which we denote by $\mathbf{m}_<$, having an approximate normalized cost of 0.67. In this work we consider five sets of 'good' rupture models, namely all rupture models having cost less than or equal to $1.005C(\mathbf{m}_<)$, $1.01C(\mathbf{m}_<)$, $1.02\,C(\mathbf{m}_<)$, $1.03\,C(\mathbf{m}_<)$, and $1.04\,C(\mathbf{m}_<)$. These sets of models are referred to as the 0.5%, 1%, 2%, 3% and 4% model ensembles below.

It is important to note that our decision to consider no ensembles larger than the 4% ensemble is entirely arbitrary. Ideally, one would want to consider the largest ensemble that fits the data 'within the error bounds.' However, the current practice of waveform inversion does not yield this information. The main problem is that there is currently no quantitative way to determine when a waveform fit is unacceptably bad. Often in data analysis the data are noisy, the noise has a known standard deviation, and the theory being fit is perfectly accurate. In that case, the likelihood of a particular model can be determined from the misfits, and the model can be accepted or rejected based on the likelihood. In the case of waveform inversion, however, the strong motion data are very accurate in the period band studied, but the wave-propagation model is very inaccurate, as we saw in Figure 5. It is not yet known how to quantify the error in a Green's function and to propagate that error back into a likelihood of the rupture model. Consequently, we cannot calculate the likelihood of models within any particular ensemble, and we cannot say which ensemble is at the boundary between likely and unlikely models. In fact, the wave form fits for the 4% model ensemble are not obviously worse than for the 1% ensemble, so it might be that both ensembles are nearly equally likely, and it would be necessary to consider the 20% (for example) ensemble to find models that can be

rigorously rejected by the data. Figure 6 shows 50 randomly chosen synthetics from the two ensembles at stations NIG017 (close to 1g1) and NIG024 from one of our inversions.

We performed three inversions, all of which used the Niigata data set. The inversions differed only in that one inversion (called the *ALL* inversion below) included the KKNPP station 1g1 seismograms in the data set (in other words, used all stations), while the second inversion (called the *NoKK* inversion) excluded the 1g1 seismograms, and the third inversion (called the *Noh13* inversion) included the 1g1 seismograms but excluded NIGH13 data. We selected NIGH13 because we speculated that interpolation of ground motions at a station with nearby neighbors would be more accurate than at a spatially isolated station, and NIGH13 has the nearest neighbors (9 km) of all Niigata stations. By chance, 1g1 was farthest (22 km) from its nearest neighbors (excluding from consideration NIG018 and the other stations at the KKNPP), so consideration of 1g1 and NIGH13 bracketed the possible range of distance to neighbors.

For the inversions, observed accelerograms were integrated to velocity, and the velocity synthetics in both inversions were low-pass filtered with a sharp corner at 0.5 Hz. No high-pass filter was applied. All inversions differed from the inversion of Cirella et al. (2008) in using 'static corrections' to ensure that the observed hypocentral S waves arrived at the stations at the times consistent with the TG3 velocity model. To determine the static correction for each station, we had to identify the hypocentral S wave at each station. The subjectively estimated mean error in each pick was 0.4 s. If we want this to correspond to a phase error less than 90 degrees, then the shortest period we can model is 1.6 s. This phase error is the main reason that it would be pointless to run an inversion of the main-shock data to periods less than 1.6 s.

Table 4 shows that the seismic cost differences between the 0.5% and 4% model ensembles are quite small, consistent with the nearly identical wave form misfits of the ensembles shown in Figure 6. In fact, most of the cost difference between the 0.5% and 4% ensembles comes from the increase of the geodetic cost. In Table 4 the 'Interval Cost' is the average cost of all models contained in a particular ensemble but not

contained in a smaller ensemble; in other words for 4% it is the average cost of all models having cost between 1.03 $C(\mathbf{m}_<)$ and 1.04 $C(\mathbf{m}_<)$. For all three inversions the seismic interval cost increases only about 1-2% from the best fitting to the worst-fitting ensemble, whereas the geodetic interval costs increase by about 13-20%. We will see that this degradation of the geodetic fit, coupled with a nearly negligible degradation in wave form fit, can cause a large variation in predicted ground motions, because of the intrinsic nonuniqueness of the inversion (different rupture models can fit the observed data equally well). We will see that the linear independence of the interpolated station's Green's function correlates with the variability of the predicted ground motion. The interval cost is a useful number tying the percentage ensemble, which is an arbitrary measure of wave form and geodetic fit, to a measure of fit that anyone can calculate unambiguously for their own inversion.

Comparison of Inversion

In this section we initially concentrate on the inversions including and omitting the KK (1g1) data. Later we will consider the *Noh13* inversion. Not surprisingly, the KK seismograms are fit somewhat better when KK data are used (*ALL* inversion, Figure 7) than when the data are not used (*NoKK* inversion, Figure 8). This is shown more quantitatively in Figure 9, which shows the cost of each individual station and component for the two inversions. Note that the cost for 1g1 (rightmost column) for the *ALL* inversion is signficantly lower than the *NoKK* cost (green triangle) for the horizontal components. However, inspection of Figure 7 and Figure 8 shows that in both inversions the 1g1 synthetics significantly underpredict the data amplitude, and that the misfit (cost) of the 1g1 synthetic is higher than that of most Niigata stations. There are several reasons for these observations. First, the observed ground motions at 1g1 have considerably higher peak velocity than do the Niigata stations, but the inversion is not highly sensitive to this large amplitude because the normalized misfit function is somewhat insensitive to amplitude discrepancies, being normalized by the sum of the RMS powers of the data and the synthetics. Second, the observed main-shock data-synthetic amplitude discrepancy is probably caused by the same factor (unmodeled geologic structure) that caused aftershock synthetics to be small (Figure 5). Finally, it is

probably likely that some bound on the allowed rupture model (for example, the requirement that slip be positive, etc.) is precluding a good fit of the 1g1 data.

We note that the data are generally better fit at stations in the southwest end of the station distribution than the northwest end. We do not know the cause of this difference. It is possible that our theoretical Green's functions describe propagation more accurately in the SW direction. Interestingly, Kato et al. (2008) present evidence that the northeast end of the fault may have a northwest-dipping segment, which if true would conflict strongly with our model fault geometry and would lead to a poorly resolved slip model, and consequent poor waveform fits, around that end of the rupture.

Because absolute amplitudes of ground motion are very important to engineers, comparison of observed and synthetic peak motions in Figure 7 and Figure 8 shows that the Spudich and Miller (1990) cost function retains some sensitivity to ground motion amplitudes. Fitted seismograms are about 1/3 the observed amplitude for the largest observations (e.g. 1g1, NIG019), whereas they are about 50% larger than the observations for the smallest observed seismograms (e.g. NIGH12, NIGH09). In other words, peak synthetic amplitudes vary by about a factor of 3 when the data amplitudes vary by a factor of 9.

Response Spectra Predicted from Model Ensembles

For engineering purposes, we have made comparisons of 5%-damped spectral acceleration calculated from identically filtered observed and synthetic seismograms (low-passed with an abrupt corner at 0.5 Hz; no high-pass filter was applied). We have done this for all synthetics calculated at the Niigata stations and at 1g1 for all of the models in the various model ensembles for all three inversions. The number of models in each ensemble is shown in Table 4. Figure 10 shows an example of all the synthetic strike-parallel response spectra calculated at 1g1 for the 334 rupture models in the 1% ensemble of the *NoKK* inversion. Note that all response spectra have been calculated for 2–20 s oscillator periods. The response spectral values at periods less than 2 s have been affected by the filter applied to the time series.

We define the bias of a synthetic response spectrum to be the ratio of the observed response spectrum to the synthetic response spectrum as a function of period. We seek to answer these questions: What is the mean bias of the 1g1 synthetic response spectra from various model ensembles? Does inclusion of the 1g1 data in the *ALL* inversion reduce the bias of 1g1 synthetic response spectra (which it should)?

Figure 11 shows the mean biases of various model ensembles for the *NoKK* and *ALL* inversions. Note that a bias of unity is the ideal result. The first obvious result is that, except for the 0.5% ensemble, the mean biases of all model ensembles from both inversions are similar. The mean biases are telling us that the observed horizontal motions are substantially (factor of 2–4) larger than the synthetics, and that the observed vertical is up to a factor of 2 larger than the synthetics. Both these observations are consistent with inspection of the seismograms in Figure 7 and Figure 8. The second result is that the biases of the *ALL* inversion, including 1g1, (dashed lines) tend to be better (closer to unity) than the *NoKK* biases, which is a result we expect. The surprising result is that the bias is significantly better for only the 0.5% ensemble from the *ALL* inversion (magenta dashed line). As there are only 10 models in this ensemble (Table 4), and because these models might be very similar to each other owing to the way the inversion perturbs model parameters, this result might be a statistical fluke.

To summarize our results thus far, inclusion of the KK data in the inversion slightly improves the predictions at KK (which we would hope), but it does not solve the systematic amplitude bias. It is important to note that some of the bias comes from site effects caused by 3D geology at the KKNPP which are not correctly modeled by our 1D velocity structure, as shown by the 1D structure's inability to predict the aftershock motions. Comparison of the differences between the 1g1 and 5g1 response spectra (Figure 10) shows that these geologically induced biases can be as large as a factor of two over the extent of the power plant.

Aleatory Variability of Response Spectra Predicted from Model Ensembles

As can be seen in Figure 10, there is a distribution of predicted spectral accelerations at station 1g1 from the 334 rupture models in the 1% ensemble. Let $\sigma_{pc}^{x}(T_j)$ denote the population standard deviation of the natural log of the response spectra (for a single component of motion) calculated at location *x* and period T_j for the *pc*% model ensemble from a particular inversion. This is a form of aleatory uncertainty in the ground-motion prediction resulting from unknown aspects of the slip distribution. We categorize it as an aleatory uncertainty because the collection of unlimited amounts of data from future earthquakes will not reduce the uncertainty of this ground-motion prediction for this past earthquake. The bias, on the other hand, is to a significant extent caused by our lack of knowledge of the 3D velocity structure, which can be learned through site surveys, and can consequently be classified as epistemic uncertainty. We note that, to first order, our estimate of $\sigma_{pc}^{x}(T_j)$ is insensitive to the mismatches between predicted and observed amplitudes of motion because $\sigma_{pc}^{x}(T_j)$ is the standard deviation of a logarithm. Thus, if we were to use a Green's function at 1g1 that predicted motions five times bigger than the Green's function actually used, all the curves in Figure 10 would be elevated by a factor of five, but the standard deviation of the logs would not change.

Circles in Figure 12 show $\sigma_{pc}^{1g1}(T_j)$ for all model ensembles (0.5%, 1%, … 4%), for all periods, and for each horizontal component for the *NoKK* inversion (other symbols will be explained later). This is the scatter in the predictions caused simply by the nonuniqueness of 'good' rupture models. For brevity we will call $\sigma_{pc}^{x}(T_j)$ the nonunique prediction sigma or the nonunique prediction scatter. The scatter has two characteristics. First, the scatter declines with increasing period, which makes sense because we should be able to image the long-wavelength parts of the rupture model with less ambiguity than the short wavelength parts. Second, the scatter increases as the percentage of the model ensemble increases. We do not imply that to achieve a stable estimate of the nonunique prediction sigma it is sufficient to consider only the 4% model ensemble. Clearly, the prediction scatter must be much worse for the 100% model ensemble. We emphasize

that our ensemble cutoff at 4% was chosen arbitrarily, and such a cutoff will remain arbitrary until it is possible to put believable error bounds on rupture models.

When we examine these sigmas and their ratios, a suprising result emerges. We have seen above that addition of the KK data to the inversion data set reduces the data-synthetic misfit at 1g1, specifically the bias of the synthetic response spectra calculated at 1g1 (Figure 11) and the wave form costs (Figure 9). This is intuitively expected and would lead us to speculate that the scatter of the predicted motions at 1g1 will be reduced. However, as we will see, the surprising result is that the scatter in the predicted motions at 1g1 *increases* (for the horizontals) when the KK data are included in the inversion, and the ratio of 1g1 scatter to Niigata scatter also increases.
The quantity $\sigma_{pc}^{1g1}(T_j)$ quantifies the scatter in the predicted spectral acceleration at station 1g1 for a given component of motion and inversion. We denote an average over periods by
$\langle\sigma_{pc}^{1g1}(T_j)\rangle_T = \frac{1}{m}\sum_{j=1}^{m}[\sigma_{pc}^{1g1}(T_j)]$.

The first counterintuitive result is that the scatter in the predicted horizontal motions at 1g1 is larger when the KK data are included in the inversion data set, compared to the scatter from the *NoKK* inversion. This can be seen in Table 5, which shows the average ratio $\langle\sigma_{pc}^{1g1}(ALL)/\sigma_{pc}^{1g1}(NoKK)\rangle_T$ for all ensembles and components. The result for the 0.5% ensemble is probably not reliable because that ensemble has only 10 members for the *ALL* inversion. Table 5 shows that for the 1% ensemble, $\langle\sigma_{pc}^{1g1}\rangle_T$ for the *ALL* inversion is 17-30% larger than the same quantity for the *NoKK* inversion for the horizontal components. The opposite is true for the vertical component, for which the scatter is reduced by about 15% when KK data are included. The difference between the vertical and horizontals might be related to the large data–synthetic amplitude differential in the horizontals (Figure 7 and Figure 8). As the data at 1g1 are difficult to fit (see Figure 7) a smaller number of models fit these data (237 in the 1% *ALL* inversion ensemble, as opposed to 334 in the *NoKK* ensemble, Table 4). It is not clear why the predictions of the smaller model set should have a higher scatter.

It can be useful to normalize $\sigma_{pc}^{1g1}(T_j)$ against some other related quantities routinely generated in the inversion process, namely the scatter in the synthetic ground-motions predicted at the Niigata stations used in the inversion. We denote the scatter in the synthetic spectral acceleration at the *j*-th period predicted at the *i*-th Niigata station by $\sigma_{pc}^{N_i}(T_j)$. (The relevant component of motion and the inversion will be clear from context.) To compare the two scatters, we will examine their ratios $\sigma_{pc}^{1g1}(T_j)/\sigma_{pc}^{N_i}(T_j)$ for individual Niigata stations. We will use the following notation to denote a mean over the set of stations used as data in the inversion, for example, $\langle\sigma_{pc}^{1g1}(T_j)/\sigma_{pc}^{N_i}(T_j)\rangle_i = \frac{1}{k}\sum_{i=1}^{k}\left[\sigma_{pc}^{1g1}(T_j)/\sigma_{pc}^{N_i}(T_j)\right]$, where N_i specifically denotes the *i*-th Niigata station, and we will use double subscripts to denote means over stations and periods, $\langle\sigma_{pc}^{1g1}/\sigma_{pc}^{N_i}\rangle_{iT} = \frac{1}{m}\sum_{j=1}^{m}\langle\sigma_{pc}^{1g1}(T_j)/\sigma_{pc}^{N_i}(T_j)\rangle_i$.

It is necessary to average the sigma ratios over Niigata stations and periods because the individual station results are rather bewildering and difficult to interpret. The average over stations and periods, $\langle\sigma_{pc}^{1g1}/\sigma_{pc}^{N_i}\rangle_{iT}$, is shown in Figure 13a and Table 6 for the *NoKK* inversion.

The first possibly practically useful result of this paper can be extracted from Table 6, namely that the scatter in the predicted horizontal response spectra at 1g1 from the *NoKK* inversion is about 22% bigger than the scatter of response spectra predicted at the Niigata stations (22% from averaging the SP and SN results for all ensembles). This result says, assuming that it can be applied to other inversions, that in the case of a true interpolation of a ground motion where there is no observation, the scatter in the horizontal component interpolant can be at least 20-25% bigger than the scatter in the motions predicted from good fitting models at sites where there were observed motions that were inverted. For the vertical component, the scatter in the interpolant is about 84% bigger than the scatter of good models' predicted motions at sites where there were observations. These results are completely unaffected by the characteristics of the 1g1 data, as they were not used in

the inversion. We shall see below that the same exercise of predicting motions at NIGH13 yields the result that the scatter in the interpolated horizontal motions at NIGH13 is 78% of the scatter of the predicted motions at all other stations, a rather different result than for 1g1.

While the waveform fits are better at NIGH13 than at 1g1, ironically, the waveform fits for the M4.7 aftershock at NIGH13 (not shown) are poorer than at 1g1. While the amplitudes of the synthetic and observed S pulses agree reasonably well, the NIGH13 data have a strong coda resonance at 2 s (or shorter period) not found in our synthetics. As the generic Cirella et al. (2008) velocity structure does not follow the NIGH13 shallow structure, it is not surprising that the observed resonances are not duplicated.

Intuitively we expect that if we include KK data in the inversion, the scatter of predicted motions at 1g1 will be reduced, so that $\langle \sigma_{pc}^{1g1} / \sigma_{pc}^{N_i} \rangle_{iT}$ will be less for the *ALL* inversion than for the *NoKK* inversion. Once again our intuition fails us, as can be seen in Figure 13b and in Table 6 by comparing *ALL* inversion ratios to *NoKK* ratios. In the case of the *ALL* inversion, the scatter in predicted horizontal and vertical spectral accelerations at 1g1 is about 30% and 43% larger, respectively, than the scatter at the Niigata stations (excluding the results for the 0.5% model set, which has only 10 models).

Scatter in Predicted Motions at NIGH13

In order to better understand the causes of the scatter in predicted motions at 1g1, we perform the same exercise of omitting NIGH13 from the data set and then predicting its ground motions. We have chosen NIGH13 because it is close to two other stations, and both inverse theory and common sense lead us to believe that the prediction of NIGH13 motions should have less bias than the predictions of the 1g1 motions. However, we are also interested in the scatter in the predicted motions at NIGH13, which is more difficult to anticipate.

We performed an inversion, called the *Noh13* inversion, in which we included the 1g1 data and all Niigata data except NIGH13, for which we predicted the motions. In the following we show analogs of Figure 11 and Figure 13 for the *Noh13* inversion. Figure 14 shows the bias of station NIGH13 in inversions with (solid lines) and without NIGH13. Both inversions give about the same biases, so it is difficult to say one is better. In general the biases are a little lower at NIGH13 than they are at 1g1 (Figure 11). The lower biases are because there is a better waveform fit at NIGH13. Figure 15 shows the fits for the *ALL* inversion at 1g1 and NIGH13. Also shown are the fits at the two stations nearest to 1g1 or NIGH13. Note that the fit is good at NIGH13 and its two nearest neighbors. The fit is bad at 1g1 and its two nearest neighbors. We will return to this observation later.

Figure 16 shows the sigma at NIGH13 for various ensembles and periods, for the *Noh13* inversion. By comparison with Figure 12, for 1g1 and the *NoKK* inversion, we can see that the scatter at NIGH13 is considerably smaller at all periods than for 1g1 (note that Figure 12 has the 4% ensemble results, not in Figure 16. Note also difference in ordinate scales). Intuitively we expect that the scatter at NIGH13 should be lower than that at 1g1 because NIGH13's nearest neighbor stations are closer than 1g1's nearest neighbors. However, Figure 15 shows that the waveform fits at NIGH13's neighbors are better than the waveform fits at 1g1 and its nearest neighbors. This raises the possibility that some factor related to the inaccuracy of the 1g1 Green's functions (in other words, the bad waveform fit) somehow contributes to the larger sigma at 1g1 compared to NIGH13. We investigate this below, with the result that our intuition about the importance of proximity to neighbors is correct.

Figure 17a (inversion *Noh13*) and Figure 17b (*ALL* station inversion) are the NIGH13 versions of Figure 13a and Figure 13b, with numeric values in Table 7. Comparing these NIGH13 results with those for 1g1, it is obvious that almost all the results for NIGH13 are yellow dots (ratio < 1) and the ratios for 1g1 are greater than 1 (black dots). This might be a useful result, because this plot compares the sigma of interpolated motions at NIGH13 to a quantity that can always be calculated in any statistical inversion, the sigma

averaged over all the stations used in the inversion. (Note, we define the ensemble *S* to be the set of all stations except NIGH13, and S_i is a specific station from this set.) In general for the horizontal components of NIGH13, the sigma at NIGH13 is lower than the sigma at the other stations. Interestingly, for 1g1 (Figure 13) we got the opposite result - the scatter of predicted SA at 1g1 was greater than the scatter of SA at the stations used as data in the *NoKK* inversion, particularly at the longer periods. In fact, averaging the SP and SN values of the ratio $\langle \sigma_{pc}^{h13} / \sigma_{pc}^{S_i} \rangle_{iT}$ over all ensembles for the *Noh13* inversion, we see that the scatter in the interpolated horizontal motions at NIGH13 is 78% of the scatter of the predicted motions at all other stations.

The important question is why the interpolation is more variable at 1g1 than at NIGH13 (specifically, there is more scatter of the forward-predicted motions at 1g1 than at NIGH13). Originally we hypothesized that the interpolation would work better at NIGH13 because its nearest neighbors are closer to it than 1g1's neigbors are to 1g1. This hypothesis is supported by our results. However, Figure 15 shows that NIGH13's neighbors have better fits than 1g1's neighbors. This probably explains the lower bias of NIGH13 (Figure 14) than 1g1 (Figure 11). We must investigate whether the better waveform fit at NIGH13 and neighbors also causes the lower scatter in predicted motions at NIGH13 than at 1g1. Of course, the scatter in predicted motions at 1g1 in the *NoKK* inversion cannot be affected by 1g1 data excluded from the inversion's data set. However, it might be that the erroneous 1g1 Green's function that produces such a bad fit might be highly sensitive to small variations in the slip model, producing large scatter. To understand this problem theoretically we created a small analog ('toy') inversion that can be studied easily.

A Simplified Problem for Studying the Interpolation

We have observed that the scatter in predicted motions at 1g1 exceeds the scatter at NIGH13. We will show that that observation is related to the isolation of the 1g1 station from the other stations, rather than to the poor data fit at 1g1. To demonstrate this result, we created a toy problem that maintained the essential physics of the situation but was very simple.

Simplified geometry and wave propagation

In the following we will show how the inverted solution of an inverse problem can be the sum of vectors that are constrained by the data and vectors from the null space. Using a linear programming algorithm we will shape the null space to produce solutions that minimize or maximize the predicted data at some unobserved location. Then we will see how the range of predicted data depends on the relative proximity of stations and the data misfit. We probably could have solved this problem using algorithm BVLS of Stark and Parker (1995), but that would have not allowed us to get the insights allowed by use of the singular value decomposition.

We represented the fault as a string of isotropic point sources at locations $\mathbf{x}_i, i = 1 \ldots P$ distributed uniformly along a 38.5 km long line at 10 km depth on Cirella's fault plane, which is roughly the depth of maximum slip in her model. We used receivers at the Niigata and KK station locations. Because our observations are response spectral values, we assumed simplified narrow-band Green's functions connecting the sources and the receivers, $\mathbf{A}_{ij} = r_{ij}^{-1} \sin(\omega t_{ij})$, where r_{ij} and t_{ij} were the distance and travel time, respectively, from the *i*-th source to the *j*-th station. A 3 km/s wavespeed was assumed. For various tests ω was varied so that the fault ranged from 2 to 6 wavelengths long. More details of specific tests will be discussed after presenting the theory.

Theoretical analysis

We have

$$\mathbf{d_o} = \mathbf{Ap} \tag{1}$$

where $\mathbf{d_o}$ is a $D\times1$ vector of observed ground motion samples, $\mathbf{p}$ is a $P\times1$ vector of subfault moments, and $\mathbf{A}$ contains Green's functions. Applying a singular value decomposition to $\mathbf{A}$, we obtain the solution

$$\mathbf{p_o} = \mathbf{VS^{-1}U'd_o} \tag{2}$$

where $\mathbf{V}$ is a $P\times P$ unitary matrix, $\mathbf{U}$ is a $D\times D$ unitary matrix, $\mathbf{U'}$ is the transpose of $\mathbf{U}$, and $\mathbf{S^{-1}}$ is a $P\times D$ matrix with inverses $[s_1^{-1}\ s_2^{-1}\ \ldots s_R^{-1}]$ of the singular values $s_1, s_2, \ldots s_R$ down the diagonal, and all other elements of $\mathbf{S^{-1}}$ equal zero. Note that R is the number of retained singular values, which might be less than the number of nonzero singular values if the user chooses to discard small singular values.

The following development applies to both the cases $R < D < P$ and $R < P < D$. In (2) the term $\mathbf{a} = \mathbf{S^{-1}U'd_o}$ is a $P\times1$ vector of weights that multiply columns of V, so we can see that the solution vector $\mathbf{p_o}$ is a sum of columns of $\mathbf{V}$ multiplied by scalar weights $\mathbf{a} = [a_1\ a_2 \ldots a_R\ 0_1\ 0_2 \ldots 0_{P-R}]'$ which are determined by the data. Because only R of the singular values are nonzero, the first R columns of $\mathbf{V}$, which we place in a matrix $\mathbf{G}$, are multiplied by nonzero weights (in other words, are constrained by data) and the last P-R columns of $\mathbf{V}$, which we place in a matrix $\mathbf{N}$ are multiplied by zero weights. These last P-R columns of $\mathbf{V}$ span the null space of $\mathbf{A}$, in other words, they are components of the solution space that create no ground motions at the observation locations. Consequently, we are free to add any linear combination of the last P-R columns of $\mathbf{V}$ to the vector $\mathbf{p_o}$ in order to enforce positivity of the solution or other constraints. Thus, any solution of the form

$$\mathbf{p} = \mathbf{Ga} + \mathbf{Nb}, \quad (3)$$

where $\mathbf{a}$ is determined by the data, and $\mathbf{b}$ is a completely arbitrary P-$R \times 1$ vector, will fit the data because $\mathbf{ANb} = \mathbf{0}$. If R includes all singular values, the data will be fit exactly; if some small singular values are discarded, the data will be fit in a least-squares sense. We are free to choose $\mathbf{b}$ so that the solution $\mathbf{p}$ satisfies desired constraints. In the following we propose constraints on $\mathbf{b}$ and pose those constrains so that they can be used in a linear programming algorithm to solve for $\mathbf{b}$.

Extremize some prediction of the solution. The prediction we specifically consider is the calculation (interpolation) of ground motion at some unobserved location. It is critically important to understand the circumstances under which an interpolated ground motion is completely unconstrained by a solution derived from a data set. Our goal is to find $\mathbf{b_g}$ and $\mathbf{b_l}$ which cause, respectively, the greatest and least ground motion E at some unobserved location. We have

$$E = \mathbf{e}'\mathbf{p}, \quad (4)$$

where $\mathbf{e}$ is a $P \times 1$ vector containing the samples of the Green's functions which map solution vector $\mathbf{p}$ to as-of-yet undetermined ground motion E at some site. Using (3), $E = \mathbf{e}'\mathbf{Ga} + \mathbf{e}'\mathbf{Nb}$. Defining $k = \mathbf{e}'\mathbf{Ga}$ and $\mathbf{n} = \mathbf{e}'\mathbf{N}$, we have $E = k + \mathbf{n}'\mathbf{b}$. E is greatest and least when $\mathbf{n}'\mathbf{b}$ is greatest and least, respectively. If $\mathbf{e}$ is linearly independent of the constrained columns of $\mathbf{V}$ (in other words, $\mathbf{G}$), then $\mathbf{e}'\mathbf{N} \neq \mathbf{0}$ and the interpolated ground motion E is not constrained by the data. Rather, the only controls on E are the bounds (if any) on $\mathbf{b}$. (Such bounds on $\mathbf{b}$ would arise from constraints like positivity applied to $\mathbf{p}$.) A measure of the linear independence of a set of vectors, which is a proxy for the indeterminacy of the interpolation, is the determinant of the matrix formed by them, with small values of the determinant indicating nearly linearly dependent columns (or rows). For a square matrix the determinant is the product of the eigenvalues. As an analog of the determinant, we use the product of all of the nonzero singular values of

$\begin{bmatrix}\mathbf{A}\\ \mathbf{e}'\end{bmatrix}$. Physically, we are determining whether the Green's function $\mathbf{e}$ for the interpolated ground motion is linearly independent of all the Green's functions for the stations used in the inversion.

Positivity. To enforce positivity we require $\mathbf{p} = \mathbf{Ga} + \mathbf{Nb} \geq \mathbf{0}$. Defining $\mathbf{k}^+ = \mathbf{Ga}$, we have constraint on $\mathbf{b}$

$$\mathbf{k}^+ \geq \mathbf{Nb}. \qquad (5)$$

Constrained moment. Let the notation $\sum(\mathbf{v})$ mean a sum of all the elements of the vector argument $\mathbf{v}$. Then, if we wish the solution to have a desired moment M_o, we have $M_o = \sum(\mathbf{p}) = \sum(\mathbf{k}^+) + \sum(\mathbf{Nb})$. Define scalar $k_o = M_o - \sum(\mathbf{k}^+)$ and define $\mathbf{q}$ as a $P - R \times 1$ vector whose j-th element is $q_j = \sum_{i=1}^{P} N_{ij}$. The moment constraint on $\mathbf{b}$ then becomes

$$\mathbf{q}'\mathbf{b} = k_o \; . \qquad (6)$$

Optimization problem. Thus, the final form of the optimization problem to be solved is:

Find $\mathbf{b}$ to minimize $\pm\mathbf{n}'\mathbf{b}$, subject to $\mathbf{k}^+ \geq \mathbf{Nb}$ (5) and $\mathbf{q}'\mathbf{b} = k_o$ (6). The optimization is performed twice, once finding $\mathbf{b_g}$ which minimizes $-\mathbf{n}'\mathbf{b}$, yielding the greatest possible predicted motion E_g, and once finding $\mathbf{b_l}$ which minimizes $+\mathbf{n}'\mathbf{b}$, yielding the least predicted motion E_l.

We solve the problem numerically by performing the singular value decomposition with Matlab function *svd*, yielding the compete $\mathbf{V}$ matrix which we partition into matrices $\mathbf{G}$ and $\mathbf{N}$. The optimization problem is solved using Matlab function *linprog*. We probably could have solved (1), augmented by the positivity, moment, and extremization constraints, directly with *linprog*. In that case we would have obtained the minimum L1-norm solution and data fits, rather than the L2-norm achieved using the svd. However,

using the svd solution allows us to calculate the determinant, which we relate to the theoretical variability of the interpolated ground motion.

Constraint equations (5) and (6) can be applied to a time-domain inverse problem of the form shown in Hartzell and Heaton (1983, their Figure 11), provided that it is possible to take the svd of the *A* matrix. Assuming that the problem is small enough to be solved by linear programming, the interpolation equation (4) can be extremized. However, in this case it is the value of the predicted seismogram at a specific time step that will be extremized. One could conceive of solving one linear programming problem for each time step of the predicted seismogram, but this may be rather cumbersome. The same restriction would apply to the use of BVLS by Stark and Parker (1995).

Results of the Simplified Inversion Tests

The question to be answered is whether the larger scatter of predicted ground motions at 1g1 compared to predictions at NIGH13 was caused by the relative isolation of the 1g1 station or because of some factor related to the poor fit of its predicted motions and the observations. We performed a series of tests summarized in Table 8. Referring to the columns of Table 8, each *test* performed N_i pairs of constrained inversions of a data set generated from a random source model satisfying the moment and positivity constraints. Each pair of inversions consisted of an optimization which minimized the predicted motion E and an optimization maximizing E. In some tests (3 - 5) random noise of amplitude *noisefr* times the max value of all the data was added to each datum. In some tests (3, 5) the noise at 1g1 was strongly boosted in order to try to get a bad misfit at 1g1. In each test except 3, one of (1g1, NIGH13) was included in the data set being inverted while the other station was omitted, and the pair of optimizations yielded E_l and E_g, the lower and upper limits of the omitted station's predicted ground motion. For each test, this yielded N_i values of $E_g - E_l$, the range of predicted (interpolated) motion at the omitted station location, and the mean value of this range is listed under *pred range*. The rms misfit over all stations and iterations is listed under *data misfit*, and the rms misfits of 1g1 and NIGH13 stations, when used in the inversions, is listed under *1g1 misfit* and *h13*

misfit. In some tests (1, 2) the rank R of the matrix was full (= number of data D), in which case the data were fit exactly, and in some tests the rank R was selected to be unity, in other words, only one singular value was retained, and data were fit approximately. In tests 1 and 2 ω was chosen so that the fault was approximately 6 wavelengths long, and P was chosen so that there were 6 point sources per wavelength (in other words, $P = 36$). This yielded tests with many more parameters than data, in which case the data were fit exactly. In order to test the effect of data misfit on predictions, in tests 3 - 5 ω was chosen so that the fault was approximately 2 wavelengths long, and P was chosen so that there were 4 point sources per wavelength (in other words, $P = 8 < D = 13$ or 14). For these tests R was set to 1 so that there was ample data misfit. Even so, a huge amount of noise had to be added to the 1g1 datum (tests 3, 5) in order to generate a large misfit at 1g1.

We have previously speculated that if the interpolation kernel (Greens function) **e** is linearly independent of the Green's functions of the other stations, the interpolated ground motion E is not constrained by the data. We also stated that a measure of the linear independence of a set of vectors, which is a proxy for the indeterminacy of the interpolation, is the determinant of the matrix formed by them. Tests 1 and 2, in which the data are fit perfectly, are consistent with this suggestion. In test 1, the station 1g1 datum was included, and the determinant was 1.06e5, which is greater than the determinant of test 2, 0.5e5, in which NIGH13 was included. This indicates that the 1g1 (simplified) Green's function is more linearly independent (of the other stations' Green's functions) than is NIGH13's, and the prediction range for 1g1 is 6.46, which exceeds the 2.01 prediction range for NIGH13.

Adding noise to the 1g1 data does not change this situation. In test 5 the 1g1 misfit is 1.73, which is much greater than the 0.29 misfit of NIGH13 in test 4. Nonetheless, the prediction range for 1g1 in test 4 is 12.4, much greater than the prediction range of 3.04 for NIGH13 in test 5. Once again, large determinant (6.20 in test 5 when 1g1 is included) corresponds to large prediction range for 1g1 (12.4 in test 4). Other tests, not shown, support this observation.

Consequently, we have concluded that the large scatter in predicted 1g1 motions (in the real inversions) is related to the linear independence of 1g1's Green's functions rather than any factors related to the poor waveform fit of the 1g1 data (Figure 15). This linear independence simply means that the simplified 1g1 Green's function is strongly different from the Green's functions of the other stations, most likely because 1g1 has no nearby station neighbors.

Comparison with Other Sources of Aleatory Variability

In this section we compare the nonunique prediction scatter at 1g1 with five other research groups' estimates of aleatory variability caused by lack of advance knowledge of earthquake source properties in kinematic or dynamic rupture modeling. Table 9 summarizes the studies we examined, the computational methods used, and the parameters varied. We include only those studies reporting statistics on 5% spectral acceleration in a period band close to ours. It is somewhat difficult to compare the methods owing to their differing choices of random parameters and their differing ways of presenting the results.

Circles in Figure 12 are σ_{pc}^{1g1} for different model ensembles from the *NoKK* inversion. It should be recalled that the wave form fits for the 4% model ensemble are not obviously worse than for the 1% ensemble (Table 4, Figure 6), and that it is not yet possible to state which ensemble (4%? 10%? 50%?) yields an unacceptable misfit to the observed seismograms.

Causse et al. (2008) used the EGF technique to estimate the median SA and its standard deviation at a soil site OGDH in Grenoble valley based on an ensemble of earthquake source parameters that sucessfully simulated the same ground motion parameters at a nearby rock site OGMU. They used a 'screened parameter input' approach, in which they restricted the range of allowable source parameters (their Table 2). To generate 10

vectors of source parameters they first generated 10 SA(f) curves corresponding to 10 deciles of predicted SA from Ambraseys et al. (1996), then they generated 9000 simulations and chose the 10 simulations closest to the 10 decile SAs. These 10 simulations provided the 10 source parameter vectors used. They used the Kolmogorov-Smirnov test to infer the median SA and standard deviation from the 10 simulated SAs (their Figure 8b), and they showed that the simulations' median and standard deviation were close to Ambraseys' (their Figure 9a) at the rock site. They then used the 10 source parameter vectors to generate motions on the soil site (their Figure 9b), from which we inferred the scatter in SA, which in this case is a true single-station measurement.

Pavic et al. (2000) used EGF summation to study the median and variability of ground motions predicted for a hypothetical (target) M 6.5 event at two Swiss stations, SLAE and SBAT. They considered two sources of variability in the predicted motions: (1) uncertainties in the source properties of the EGF event, and (2) variability in the source properties of the hypothetical event (see Table 9 for a list of properties). To assess the EGF errors, they asked an expert panel to give 'optimistic' and 'pessimistic' estimates of errors in EGF parameters such as seismic moment, static (Brune's) and dynamic stress drop, fault size (characteristic length), dip and strike angles. For subsequent analysis, they used means of the optimistic and pessimistic error estimates (their Table 1). For the target event variability, they themselves estimated bounds on the following target event parameters: stress drop, strike, dip, S-wave velocity in the fault area, rupture velocity, the shape factor (length over width) of the fault (assumed rectangular) as well as the relative point of nucleation within the fault area (their Table 3). For the target M = 6.5 event they had EGFs at SLAE (r = 14 km) and SBAT (r = 61 km). Simulation SLAE1 used the SLAE EGF and simulation SBAT1 used the SBAT EGF. Both simulations used uncertainties in their Table 3. For simulation SBAT2, they truncated the input distributions in their Table 3 at about 2 standard deviations. In Figure 12 we use results from their Table 4.

Pitarka et al. (2002) studied aleatory variability in ground motions calculated for kinematic rupture models and theoretical Green's functions using the method of Pitarka et

al. (2000), a mixed deterministic-stochastic method. Fourteen scenario rupture models were used (summarized in their Table 2), in which each varied usually only one of the source properties in Table 9 (which we will call the 'primary' source properties), with ground motions calculated at 30 - 52 stations at constant R_{jb}. For each scenario there were 12 realizations of the scenario (two slip models × two depths to top of rupture × three mechanisms). Pitarka et al. (2002) report the median and standard deviation of the predicted ground motion for each scenario. However, since a 'primary' source property like rupture velocity did not vary within the 12 realizations of any scenario, we must look at the difference in motions between scenarios to see the effects of varying primary source properties on the predicted ground motions. As a proxy for source-related variation in ground motion, in Figure 12 we used the log of the ratio of their mean SA for the 'Med' scenario over the mean SA of their 'Max1' scenario. They believed the 'Med' scenario to be a reasonable median motion earthquake, having fixed median values of rupture area, rise time, rupture velocity, slip contrast, and hypocenter location. They believed their 'Max1' scenario to have a combination of source parameters (median rupture area, short rise time, large rupture velocity and slip contrast, and unilateral rupture) that caused large but not extreme ground motions.

Priolo et al. (2003b) used the EXWIM 2.1 method (Priolo et al., 2003a), a mixed deterministic-stochastic method for ground motion simulation. They used 5 different slip distributions and 153 different hypocenters, for a total population of 765 three-component seismograms at each site. They simulated a M6.5 strike-slip and a M6.5 dip-slip quake. The strike-slip quakes had groups of 11 sites at each of a set of Rjb distances, and the dip-slip quake had groups of 20 sites at each distance. Our estimate of aleatory sigma was formed for each mechanism (strike-slip or dip-slip), period, and distance by forming the mean, over all 11 or 20 stations at constant Rjb, of the logs of the ratios of [the mean value of the predicted motion (blue dot)] over [the minus-one-standard deviation motion (lower red triangle)] reported in their Figures 13-17 and 22-26. Consequently, our estimate of aleatory sigma includes some scatter from using multiple sites.

Unlike the above kinematic studies, Ripperger et al. (2008) generated source variability by using ensembles of 30 or 61 randomly variable initial stress distributions, which were input into dynamic rupture simulations to generate the variable slip models for simulated ruptures of M6.7 - 6.9, from which ground motions were generated. The ensemble of 30 rupture models all had the same hypocenter, so the variability of ground motion for this ensemble resulted directly from variations in the slip distribution and slip-velocity function. The ensemble of 61 rupture models had different hypocenters, so their ground motions display greater variability owing to directivity. Average stress-drops vary by a factor less than two among the individual rupture models. Ground motions for each of the ensembles were calculated at groups of about 11 sites having constant R_{jb}. As our aleatory sigma we take their interevent variability σ_e averaged over sites at constant R_{jb}.

For comparison we have added to Figure 12 estimates of interevent standard deviation τ_o (red dashed line) and total scatter $\sqrt{(\tau_o^2 + \sigma_o^2)}$ (blue dashed line), where σ_o is intraevent standard deviation, for firm rock sites having linear soil response for a M6.5 event, from the empirical ground-motion prediction relation of Abrahamson and Silva (2008). τ_o characterizes the earthquake-to-earthquake variation caused by factors such as differing stress drop; σ_o contains the site-to-site variation of ground motion for a single quake, caused by factors such as variable directivity at each site. We have specifically omitted from our total scatter the term σ_{amp}, which is meant to characterize the site-to-site variation of soil amplification, a factor not present in the numerical simulations.

The first obvious result in Figure 12 is that almost all of the aleatory scatter values of the ground motions from kinematic rupture models exceed the blue dashed line, which is the empirically observed scatter in response spectra, excluding the effects of variable soil amplification. Clearly these kinematic rupture models contain too much source variability. Abrahamson (personal communication) has speculated that real earthquake ruptures have correlated source properties (for example, local rupture velocity and peak slip velocity at the same point, for example) that are not present in the kinematic rupture models, leading to excessive variation in the kinematic rupture models and resulting ground motion.

The second result is that the aleatory variation of Ripperger's ground motions is much smaller than that of the kinematic rupture models, indicating that the correlations of source properties in dynamic models do result in lower ground motion variability, although we must bear in mind that Ripperger's variability of stress drop is less than a factor of two – in other words, rather low.

The third result is that Ripperger's variability is comparable to the empirical variability. Abrahamson and Silva's blue dashed line (Figure 12) includes the effects of variable source properties (for example, stress drop) as well as variations like directivity amplification that vary from site to site in a single earthquake. Ripperger's variability for variable hypocenter location agrees rather well with the blue dashed line. However, Ripperger's result for fixed hypocenter is a bit bigger than the empirically observed earthquake-to-earthquake variation (red dashed line), despite Ripperger's rather small stress drop variation.

The fourth result is that our nonuniqueness scatter at 1g1 for the 4% model ensemble approaches Abrahamson and Silva's observed interevent scatter. This means that the nonuniqueness variability of predicted motion at 1g1 is almost as great as the variability of motion incurred by using a different earthquake having the same magnitude and hypocenter to predict the motion at 1g1. (We make the 'same hypocenter' restriction because differences in directivity contribute to the intraevent error that is characterized by the 'total' sigma curve in Figure 12.) Of course, this observation depends on the choice of the 4% ensemble, which is arbitrary. However, recall that the 4% model ensemble misfit is not obviously worse than the 1% ensemble's misfit (Figure 6). It may be possible that some wave form inversions of strong motion data have misfits substantially exceeding the 4%-ensemble level, meaning that spectral acceleration predictions based on these inversions might be more inaccurate than simply predicting the spectral acceleration from a GMPE such as Abrahamson and Silva (2008) with a directivity correction (for example, Somerville et al., 1997).

It is not clear whether the nonunique prediction scatter should be added to the other sources of aleatory variability in the studies summarized in Table 9. None of those studies used a rupture model inferred for a real earthquake. On the other hand, if one of the randomly chosen slip models happened to agree exactly with a particular earthquake's rupture model, for example the Wald and Heaton (1994) Landers earthquake rupture model, it would be clear that the nonunique prediction scatter should be added to the aleatory variability.

Conclusions

We have calculated the scatter in predictions of SA at 1g1 and NIGH13 based on the nonuniqueness of rupture models. This is a hitherto uninvestigated source of aleatory variability that should be included in studies of aleatory variability which use observed slip distributions with randomized hypocenters. We saw that the bias of the predicted ground motion at 1g1 and 5g1, presumably caused by a poor wave propagation model, was much larger than the nonunique prediction scatter, emphasizing the importance of a good propagation model. This scatter behaves nonintuitively; including the 1g1 data in the inversion lowers the bias of predicted 1g1 motions, an unsurprising result, but we got the nonintuitive result that including the 1g1 data in the inversion increases the scatter in the predicted 1g1 motions, whereas including NIGH13 data in the inversion slightly reduced its scatter. In addition, the ratio of 1g1 scatter to Niigata scatter also increased, whereas the opposite result was obtained for NIGH13 scatter. The first possibly practically useful result of this paper for shake-map purposes can be extracted from Table 6, namely that the scatter in the predicted horizontal response spectra at 1g1 from the *NoKK* inversion is about 22% bigger than the scatter of response spectra predicted at the Niigata stations. This result says, assuming that it can be applied to other inversions, that in the case of a true interpolation of a ground motion where there is no observation, the scatter in the horizontal component interpolant can be 22% bigger than the scatter in the motions predicted from good fitting models at sites where observed motions were inverted. We saw that the scatter in the predicted motions was related to the linear

independence of a station's Greens functions, which is greater for more spatially isolated stations. We compared our nonuniqueness scatter with aleatory variation of ground motions from kinematic and dynamic rupture models. Almost all of the aleatory scatter values of the ground motions from kinematic rupture models exceed the empirically observed scatter in response spectra from a standard GMPE (Abrahamson and Silva, 2008), excluding the effects of variable soil amplification. Clearly these kinematic rupture models contain too much source variability. The aleatory variation of Ripperger's dynamic rupture ground motions is much smaller than that of the kinematic rupture models, indicating that the correlations of source properties in dynamic models result in lower ground motion variability. Ripperger's aleatory variability of ground motion is comparable to the empirical variability from Abrahamson and Silva (2008). Finally, our nonuniqueness scatter at 1g1 for the 4% model ensemble approaches Abrahamson and Silva's observed interevent scatter. This means that the variability of predicted motion at 1g1 caused by nonuniqueness in the rupture model is almost as great as the variability of motion incurred by using a different earthquake having the same magnitude and hypocenter to predict the motion at 1g1 (we add the stipulation of same hypocenter because Abrahamson and Silva's interevent variability does not include the effects of directivity, which would contribute to the neglected intraevent variability). Additionally, we found that our nonuniqueness scatter at 1g1 for the 4% model ensemble approaches Abrahamson and Silva's observed interevent scatter. However, in practice the nonuniqueness scatter could be greater than we have shown because our choice of a maximum 4% ensemble was arbitrary, and it is impossible at this time to choose an ensemble of 'good' models objectively.

Finally, while the the bias of interpolated ground motions has not been our main topic of investigation, the biases are of first order importance in the estimation of ground motion at a particular site using interpolation of motion from surrounding stations. Figure 11 shows that the observed motions at the KKNPP were as much as four times larger than our interpolated motions, and Figure 14 shows a bias ranging between factors of 0.5 and three at NIGH13. From the modeling of aftershocks at KKNPP (Figure 5) it could be anticipated that the interpolated motions would be smaller than the actual motions. This

underestimation is probably caused by our poor model of geologic structure under the plant, and it points out the acute need to record ambient seismicity (M > 4.0) on-site at critical facilities in order to have data that can be used to understand actual, rather than presumed, site amplifications.

Data and Resources

The F-net Broadband Seismograph Network mechanism catalog was searched using www.fnet.bosai.go.jp/event/search.php?LANG=en (last accessed on May 4, 2011). Matlab is software from the Mathworks (www.mathworks.com). Accelerograms from the KKNPP were provided on a CD by the Association of Earthquake Disaster Prevention, 5-26-20 Shiba, Minato-ku, Tokyo, 108-0014 Japan, office@aedp-jp.com, which is the sole distributor of such data. Copyright of all KKNPP data belongs to the Tokyo Electric Power Company.

Acknowledgments

We thank the Association of Earthquake Disaster Prevention for providing the database of main shock and aftershock data at the Kashiwazaki-Kariwa Nuclear Power Plant. We thank Dr. Kenishi Tsuda of Shimizu Corporation for providing insight into sources of information for this study, and we thank Dr. Arben Pitarka and Enrico Priolo for providing unpublished supplementary materials. We thank Drs. D.M. Boore and J. Ake for their helpful reviews. This work was supported by the U.S. Nuclear Regulatory Commission (NRC) Office of Research Job Code N6501. The conclusions in this report represent those of the authors and are not necessarily those of the NRC. Any use of trade, product, or firm names is for descriptive purposes only and does not imply endorsement by the U.S. Government.

References

Abrahamson, N, and W. Silva, 2008. Summary of the Abrahamson and Silva NGA ground motion relations, Earthq. Spectra, 24, 67-96, doi: 10.1193/1.2924360.

Ambrayseys, N., K.A. Simpson, J.J.Bommer, 1996. Prediction of horizontal response spectra in Europe, Earthq. Eng. Struct. Dyn., 25, 371-400.

Brocher, T.M., 2005. Empirical relations between elastic wavespeeds and density in the Earth's crust, Bull. Seismol. Soc. Am., 95, 2081–2092.

Causse, M., F. Cotton, C. Cornou, and P-Y. Bard, 2008. Calibrating median and uncertainty estimates for a practical use of empirical Green's functions technique, Bull. Seismol. Soc. Am., 98, 344-353, doi: 10.1785/0120070075.

Cirella, A., A. Piatanesi, E. Tinti, and M. Cocco, 2008. Rupture process of the 2007 Niigata-ken Chuetsu-oki earthquake by non-linear joint inversion of strong motion and GPS data, Geophys. Res. Lett., 35, L16306, doi:10.1029/2008GL034756.

Hartzell, S. H. and T. H. Heaton, 1983. Inversion of strong ground motion and teleseismic waveform data for the fault rupture history of the 1979 Imperial Valley, California earthquake, Bull. Seismol. Soc Am., **73**, 1553-1583.

Hudnut, K. W., Z. Shen, M. Murray, S. McClusky, R. King, T., Herring, B. Hager, Y. Feng, P. Fang, A. Donnellan, and Y. Bock (1996). Co-seismic displacements of the 1994 Northridge, California, earthquake, Bull. Seism. Soc. Am., 86**,** 1B, S19-S36

Ji, C., D.J. Wald, and D.V.Helmberger, 2002. Source description of the 1999 Hector Mine, California, earthquake, Part I: Wavelet domain inversion theory and resolution analysis, Bull. Seismol. Soc. Am., 92, 1192-1207.

Kato, A., S. Sakai, E. Kurashimo, T. Igarashi, T. Iidaka, N. Hirata, T. Iwasaki, T. Kanazawa, and Group for Aftershock Observations of the 2007 Niigataken Chuetsu-oki earthquake, 2008. Imaging heterogeneous velocity structures and comples aftershock distributions in the source region of the 2007 Niigataken Chuetsu-oki earthquake by a dense seismic observation, Earth, Planets, Space, **60**, 1111-1116.

Liu, P., S. Custodio, and R. Archuleta, 2006. Kinematic inversion of the 2004 M 6.0 Parkfield earthquake including an approximation to site effects, Bull. Seismol. Soc. Am., 96, S143-S158, doi:10.1785/0120050826.

Olson, A.H, and R.J. Apsel, 1982. Finite faults and inverse theory with applications to the 1979 Imperial Valley earthquake, Bull. Seismol. Soc. Am., 72, 1969-2001.

Parker, R.L., 1994. Geophysical Inverse Theory. Princeton University Press, Princeton,

NJ.

Pavic. R., M. Koller, P-Y. Bard, and C. Lacave-Lachet, 2000. Ground-motion prediction with the empirical Green's function technique: an assessment of uncertainties and confidence level, J. Seismol., 4, 59–77.

Piatanesi, A., A. Cirella, P. Spudich, and M. Cocco, 2007. A global search inversion for earthquake kinematic rupture history: Application to the 2000 western Tottori, Japan earthquake, J. Geophys. Res., 112, B07314, doi:10.1029/2006JB004821.

Pitarka, A., P. Somerville and N. Collins, 2002. Numerical simulations for evaluation of median and upper limit ground motions in Switzerland, Unpublished report, URS Corporation, Pasadena.

Pitarka, A., P.G. Somerville, Y. Fukushima, T. Uetake, and K. Irikura, 2000. Simulation of near-fault strong-ground motion using hybrid Green's functions, Bull. Seism. Soc. Am., 90, 566-586.

Priolo, E., A. Vuan, P. Klinc, and G. Laurenzano, 2003a. Estimation of the median, near fault ground motion in Switzerland, Scientific Report N. 5, PEGASOS Project, Rel. OGS-21/2003/CRS-2.

Priolo, E., A. Vuan, P. Klinc, and G. Laurenzano, 2003b. Estimation of the median, near fault ground motion in Switzerland, Final report N. 8, PEGASOS Project, Rel. OGS-33/2003/CRS-4.

Ripperger, J., P.M. Mai, and J.-P. Ampuero, 2008. Variability of near-field ground motion from dynamic earthquake rupture simulations, Bull. Seismol. Soc. Am., 98, 1207-1228.

Somerville, P.G., Smith, N.F., Graves, R.W., and Abrahamson, N.A., 1997. Modification of empirical strong ground motion attenuation relations to include the amplitude and duration effects of rupture directivity, Seismol. Res. Let. 68, 199-222

Spudich, P., and D.P. Miller, 1990. Seismic site effects and the spatial interpolation of earthquake seismograms: Results using aftershocks of the 1986 North Palm Springs, California, earthquake, Bull. Seismol. Soc. Am., 80, 1504– 1532.

Spudich, P., and L. Xu, 2003. Software for calculating earthquake ground motions from finite faults in vertically varying media, IASPEI *Handbook of Earthquake and Engineering Seismology* , Part B, pp. 1633-1634, Academic Press, with associated software on accompanying CD.

Stark, P.B. and R.L. Parker, 1995. Bounded-variable least-squares: an algorithm and applications. Comp. Stat., 10, 129-141.

Tokyo Electric Power Company (TEPCO), undated. CD-ROM:*Acceleration-Time History Waveforms of Niigata-Chuetsu-Oki Earthquake Collected at Kashiwazaki-Kariwa Nuclear Power Station*, (data time series and associated text metadata files), distributed by Association for Earthquake Disaster Prevention, 5-26-20 Shiba, Minato-ku, Tokyo, 108-0114 Japan.

Tokyo Electric Power Company (TEPCO), 2008. Report of evaluation of observed ground motion on 2007 Chuetsu-Oki earthquake and Ss ground motion on the Kashiwazaki-Kariwa Nuclear plant. (Submitted to the Nuclear and Industrial Safety Agency on Sep. 24, 2008) (in Japanese). www.**tepco**.co.jp/nu/material/files/g08060602.pdf, p. 31, last accessed 14 September 2011.

Wald, D.J., and T.H. Heaton, 1994. Spatial and temporal distribution of slip for the 1992 Landers, California, earthquake, Bull. Seismol. Soc. Am., 84, 668-691.

Watanabe T., T. Moroi, R. Tokumitsu, I. Nishimura., and K. Hijikata, 2011. Examination of relation between locations of asperities and site amplification characteristics of ground motions by analysis considering the folded structure - Estimation based on the strong motion records obtained from the 2007 Niigataken Chuetsu-Oki earthquake in the Kashiwazaki-Kariwa nuclear power station, J. Struct. Constr. Eng., AIJ, 76, 71-78, (Japanese with English abstract)

Author Affiliations

Paul Spudich
U.S. Geological Survey
345 Middlefield Road
Menlo Park, CA 94025 USA
+1-650-329-5654
spudich@usgs.gov
(Corresponding Author)

Antonella Cirella
Istituto Nazionale di Geofisica e Vulcanologia
Via di Vigna Murata, 605
00143 Roma, ITALY
+39 0651860545
antonella.cirella@ingv.it

Tables

Table 1. Simplified geology at KKNPP boreholes

Formation name	**Description (simplified)**	**Depth to top of layer (m)**		
		g07-g10	**g51-g55**	**sg1-sg5**
(Top layer)	Replacement sand	0	-	0
Banjin	Medium sand	-	-	15
Yasuda	Silt, clay, sand	6	0	70
Nishiyama	Mudstone, sandstone	72	28.6	83
Shiiya	(Undescribed)	-	101.2	-
	(Bottom of hole)	300	300	250

Table 2. Velocity model TG3

Depth (km)	**Vp (km/s)**	**Vs (km/s)**	**Density (g/cm3)**
0.000	1.500	0.3158	2.000
0.0594	1.860	0.5187	2.000
0.1966	2.170	0.7243	2.020
0.2968	2.330	0.8495	2.060
0.4974	2.350	0.8651	2.065
0.8219	2.520	1.0011	2.100
1.1966	2.860	1.2918	2.170
1.5158	3.340	1.7145	2.255
1.7982	3.480	1.8346	2.280
2.2625	3.670	2.0064	2.315
2.6847	3.970	2.256	2.365
3.3179	4.4626	2.5765	2.430
3.872	4.8902	2.8234	2.490
4.7427	5.2687	3.0419	2.545
5.996	5.7919	3.344	2.640

9.000	5.810	3.350	2.700
12.00	5.890	3.400	2.800
15.00	5.970	3.450	2.900
255.0	7.400	4.200	3.200

Table 3. Main shock and aftershocks recorded at KKNPP

Origin, UTC (2007)	**Origin, JST (2007)**	**M**	**Mo**	**F-net mechanism**
7/16,0113	7/16,1013	Mw 6.6	9.3e18	Str 215;49 dip 49;42 rake 80;101
7/16,0200	7/16,1100	Mjma 3.7		
7/16,0637	7/16,1537	Mw 5.6	3.26e17	Str 219;24, dip 47;44, rake 100;79
7/16,0842	7/16,1742	Mw 3.5	2.09e14	Str 309; 211, dip 78;54, rake 37;166
7/16,1208	7/16,2108	Mw 4.4	5.21e15	Str 187;39, dip 54:41, rake 70;115
7/24,2152	7/25,0652	Mw 4.7	1.18e16	Str 25;203, dip 49;41, rake 92;88
8/03,1516	8/04,0016	Mjma 3.2		

Table 4. Number of models, average and interval costs per seismogram for each model ensemble and inversion

Ens.	**Inversion**								
	NoKK			**ALL**			**Noh13**		
	N	**Seis. Int. Cost**	**Geod. Int. Cost**	**N**	**Seis. Int. Cost**	**Geod. Int. Cost**	**N**	**Seis. Int. Cost**	**Geod. Int. Cost**
0.5%	122	0.5886	0.0856	10	0.6121	0.0833	73	0.6320	0.0816
1%	334	0.5894	0.0882	237	0.6146	0.0847	269	0.6337	0.0841
2%	1534	0.6034	0.0810	1584	0.6180	0.0868	1724	0.6348	0.0892
3%	4897	0.6008	0.0914	4179	0.6223	0.0905	4705	0.6371	0.0944
4%	8561	0.6012	0.0989	8442	0.6215	0.0987	8516	0.6373	0.1015

Table 5. Ratio of 1g1 scatter for ALL and NoKK inversion, averaged over period

pc, %	$\langle \sigma_{pc}^{1g1}(ALL)/\sigma_{pc}^{1g1}(NoKK)\rangle_T$		
	SP	**SN**	**UD**
0.5	0.7954	0.7529	0.3386
1	1.3024	1.1704	0.8521
2	1.0579	1.0814	0.8158
3	1.0393	1.0522	0.8998
4	1.0053	0.999	0.9549

Table 6. Ratio of 1g1 to average Niigata station scatters, ALL and NoKK inversions, averaged periods

Inversion	**pc, %**	$\langle \sigma_{pc}^{1g1}/\sigma_{pc}^{N_i}\rangle_{iT}$		
		SP(X)	**SN(Y)**	**Z**
NoKK	0.5	0.9096	1.3896	2.2108
NoKK	1	1.1243	1.2633	2.0944
NoKK	2	1.1843	1.2526	1.7229
NoKK	3	1.2086	1.3022	1.6153
NoKK	4	1.2273	1.3127	1.5585
ALL	0.5	1.7304	2.1941	1.2919
ALL	1	1.2466	1.3266	1.3486
ALL	2	1.2886	1.3535	1.3759
ALL	3	1.2961	1.3777	1.4811
ALL	4	1.2605	1.2792	1.4944

Table 7. Ratio of Nigh13 to average of other station scatters, averaged over periods

Inversion	**%**	$\langle \sigma_{pc}^{h13}/\sigma_{pc}^{S_i}\rangle_{iT}$		
		SP(X)	**SN(Y)**	**Z**
ALL	0.5	1.2535	0.9774	1.3438
ALL	1.0	0.9296	0.6230	0.8765
ALL	2.0	0.8490	0.6154	0.7684
ALL	3.0	0.8475	0.6549	0.7374
Noh13	0.5	1.0432	0.7066	1.1161
Noh13	1.0	0.8608	0.6775	0.9464
Noh13	2.0	0.7772	0.6977	0.8128
Noh13	3.0	0.7851	0.6990	0.7812

Table 8. Results of 'toy' inversion tests

test #	**N_i**	**inv stn**	**pred stn**	**noisefr**	**1g1 noise boost %**	***R***	***D***	***P***	**det**	**data misfit**	**1g1 misfit**	**h13 misfit**	**pred range**
1	100	1g1	h13	0	0	13	13	36	1.06e5	0	0		2.01
2	100	h13	1g1	0		13	13	36	0.5e5	0		0	6.46
3	300	all	none	0.01	100	1	14	8	8.04	1.00	1.44	0.43	
4	300	h13	1g1	0.01		1	13	8	1.62	1.57		0.29	12.4
5	1000	1g1	h13	0.01	200	1	13	8	6.20	2.21	1.73		3.04

N_i = number of pairs of constrained inversions of a data set. *inv stn* = which of 1g1/NIGH13's datum was included in the inversion. *pred stn* = the station for which lower and upper bound ground motions E_l and E_g were predicted. *noisefr* = fractional noise added to all data. *1g1 noise boost* = percent boost of noise at 1g1. R = number of retained singular values. D = number of data inverted. P = number of parameters in the model. *det* = determinant of the SVD, *data misfit* = rms value of data misfit over all stations and realizations. *pred range* = mean value of $E_g - E_l$. *1g1 misfit* = rms value of the misfit of the 1g1 datum over all realizations. *h13 misfit* = rms value of the misfit of the NIGH13 datum over all realizations.

Table 9. Summary of aleatory sigma studies for kinematic and dynamic rupture models

Source	M	Rjb (km)	T (s) [1]	Method	Variable parameters	Used in **Figure 12**
Causse et al. (2008)	5.5	15	1	EGF summation	Target/EGF stress drop ratio Rupture velocity Hypocenter location Fault aspect ratio Target rake	Soil sigma at a single site at1 Hz measured from their Figure 9b
Pavic et al. (2000)	6.5	14, 61	1, 2, 10	EGF summation	EGF Mo EGF stress drop EGF strike, dip Target stress drop Vs at target Target rupture velocity Target aspect ratio Hypocenter location Target rake	Their Table 4, single-station results for models SLAE 1, SBAT 1, and SBAT 2
Pitarka et al. (2002)	5.5, 7	5, 25, 60	1, 2, 5	Combined deterministic–stochastic method in a 1D structure	Rupture area (stress drop) Slip rise time Rupture velocity Slip contrast (roughness) Hypocenter location Mechanism (SS , RV, NL) Slip distribution Depth to top of rupture Receiver location [2]	Ln(Med/Max1) scenarios from their Figures 4 and 11.
Priolo et al. (2003b)	6.5	1, 3, 5, 10, 25	1, 2	Deterministic method in a 1D structure, with random noise in a deterministic envelope	Slip distribution Hypocenter location Mechanism (SS, DS) Stress drop	Standard deviations log-averaged over equidistant stations, from their Figures 13-17 and 22-26.
Ripperger et al. (2008)	6.7-6.9	1, 10, 30, 60	1	Dynamic rupture simulations using randomized initial stress fields with the same wavenumber spectrum and hypocenter	Phase of the initial stress field	Interevent scatter σ_e for their variable and fixed hypocenter ensembles, from their Table 5

[1]Periods considered in this paper. [2]Their reported standard deviations include variation of receiver location

Figure Captions

Figure 1.

Map of the fault geometry of the 2007 Niigata-ken Chuestu-oki, Japan earthquake. The dashed black line represents the surface projection of the fault plane adopted in this study. Black star indicates the epicenter. White triangles and inverted triangles represent K-NET (surface sensor) and KiK-net (borehole sensor) strong motion stations respectively. Black dots represent GPS stations. White dots are GPS stations not used in this study. KKNPP indicates the site of Kashiwazaki-Kariwa nuclear power plant. Inset shows the largest aftershocks' and the mainshock's magnitudes and mechanisms. From Cirella et al. (2008).

Figure 2.

The main shock and several aftershocks were recorded at surface free-field accelerographs 1g1, 5g1, and sg1. (Figure modified from TEPCO, undated).

Figure 3

Various 1D velocity structures near the Kashiwazaki-Kariwa nuclear power plant. Borehole structures are from borehole logging. The black dashed line shows the layered 1D structure inferred from the shallower 3D structure (Watanabe et al., 2011; Tepco, 2008). The solid black line is the structure used by Cirella et al. (2008). We concocted a gradient structure TG3 (dotted line) by passing a gradient through the borehole and 3D structures below the KKNPP. We called this structure TG3. Inset shows borehole structure on a larger scale.

Figure 4

Main-shock integrated accelerations recorded at free-field stations 1g1, 5g1, and sg1. Depicted time series have been filtered with an acausal high pass filter having a 0.1 Hz corner.

Figure 5

Comparison of observed and synthetic aftershock ground velocities at station 1g1. Blue is data, cosine-taper filtered from 0.05 to 0.1 Hz and 0.25 to 0.5 Hz. Red are synthetics, low-pass cosine-taper filtered from 0.25 to 0.5 Hz. Synthetic amplitudes are about half of data amplitudes.

Figure 6

Synthetic ground velocity seismograms from 50 randomly chosen rupture models in the 1% and 4% model ensembles of the *NoKK* inversion (superposed colored lines) and the observed data (dashed black lines) at stations NIG017 and NIG024.

Figure 7

Comparison of observed (blue) and fitted (red) velocity seismograms used in the *ALL* inversion (including 1g1 data). Each time series in a data-synthetic pair is scaled by a common factor that varies from pair to pair. Numbers with each trace are the peak amplitude of the observed waveforms in cm/s. Synthetics and data are low-pass filtered with a cosine taper from 0.25 to 0.5 Hz. Synthetics are calculated for the best (lowest cost) rupture model. Note that the 1g1 synthetics significantly underpredict the data.

Figure 8

Comparison of observed (blue) and fitted (red) velocity seismograms used in the inversion lacking KK data. Seismograms are scaled and filtered as in Figure 7. In the comparison for station 1g1 (bottom row), the synthetic seismogram has been forward predicted from the rupture model. Note that the 1g1 synthetics significantly underpredict the data.

Figure 9

Costs (misfits) of individual waveforms for best rupture models of the *NoKK* (circles) and *ALL* (diamonds) inversions. Each panel shows a different component of motion. Green triangle shows the cost for station 1g1 in the *NoKK* inversion, where the 1g1 synthetic is calculated by forward modelling from the best rupture model. Note that the *ALL* inversion cost for station 1g1 is less than the *NoKK* inversion, as expected, but the costs are still higher than most Niigata stations.

Figure 10

Observed and synthetic strike-parallel spectral accelerations. Observed from stations 1g1 (orange) and 5g1 (red). Thin multicolored lines are individual response spectra from each of the 334 rupture models in the 1% model ensemble from the *NoKK* inversion. Heavy dotted black line is the logarithmic mean of the synthetic response spectra calculated at 1g1. Yellow error bars are schematic illustrations of the population standard deviation of the logarithms of the response spectra at each period.

Figure 11

Mean biases (ratio of observed to synthetic response spectra) at 1g1 from the *NoKK* (solid lines) and *ALL* inversions (dashed lines). Colors indicate model ensemble.

Figure 12

Superposition of our nonuniqueness predictive scatter with aleatory variability from sources in Table 9. Symbol shape indicates source of information. Symbol size indicates magnitude of the event being modeled. Symbol color indicates Joyner-Boore distance of the site. ‘s’ and ‘d’ in Priolo’s diamonds indicate SS and DS mechanisms, respectively. 'v' and 'f' in Ripperger's triangles indicate variable and fixed hypocenter ensembles, respectively. Percentage in our results (circles) indicate model ensemble. Dashed lines are Abrahamson and Silva (2008) inter-event sigma (red) and total sigma (excluding site-to-site sigma) (blue).

Figure 13

Logarithm base-2 of the ratio $\langle \sigma_{pc}^{1g1} / \sigma_{pc}^{N_i} \rangle_{iT}$ for the different model ensembles and components of motion. Black line shows the $\log_2(x) = 0$ amplitude level; green dotted lines show the $\log_2(x) = \mp 0.5$ levels. Values of the data greater/less than unity are shown by a black/yellow dot respectively. a) Ratio for *NoKK* inversion. The scatter in the predicted horizontal response spectra at 1g1 from the *NoKK* inversion is about 25% bigger than the scatter of response spectra predicted at the Niigata stations. b) Ratio for *ALL* inversion. The scatter in predicted horizontal and vertical spectral accelerations at 1g1 is about 30% and 40% larger, respectively, than the scatter at the Niigata stations. Ratio for *ALL* inversion exceeds horizontal ratio for *NoKK* inversion in a).

Figure 14

Mean biases (ratio of observed to synthetic response spectra) at NIGH13 from the *Noh13* (solid lines) and *ALL* inversions (dashed lines). Colors indicate model ensemble.

Figure 15

Filtered velocity waveforms (red = synthetic, blue = data) from the ALL inversion. Top three rows show waveforms from NIGH13 and its two nearest neighbors nig024 and nig025. Bottom three rows show 1g1 and its two nearest neighbors, nig017 and nig019. Note that the waveform fit at NIGH13 and its neighbors is much better than at 1g1 and its neighbors.

Figure 16

σ_{pc}^{h13} for all model ensembles (0.5%, 1%, 2%, 3%), for all periods, and for each horizontal component. This is the scatter in the predictions caused simply by the nonuniqueness of 'good' rupture models. Number in each circle is the percent model ensemble, each percentage having a unique color. NIGH13 scatters are smaller than 1g1 scatters for all ensembles.

Figure 17

Logarithm base-2 of the ratio $\langle \sigma_{pc}^{h13} / \sigma_{pc}^{S_i} \rangle_{iT}$ for the different model ensembles and components of motion. Black line shows the $\log_2(x) = 0$ amplitude level. Values of the data greater/less than unity are shown by a black/yellow dot respectively. a) Ratio for *Noh13* inversion. The scatter in the predicted horizontal response spectra at NIGH13 from the *Noh13* inversion is about 25% smaller than the scatter of response spectra predicted at the Niigata stations and at 1g1. b) Ratio for *ALL* inversion.

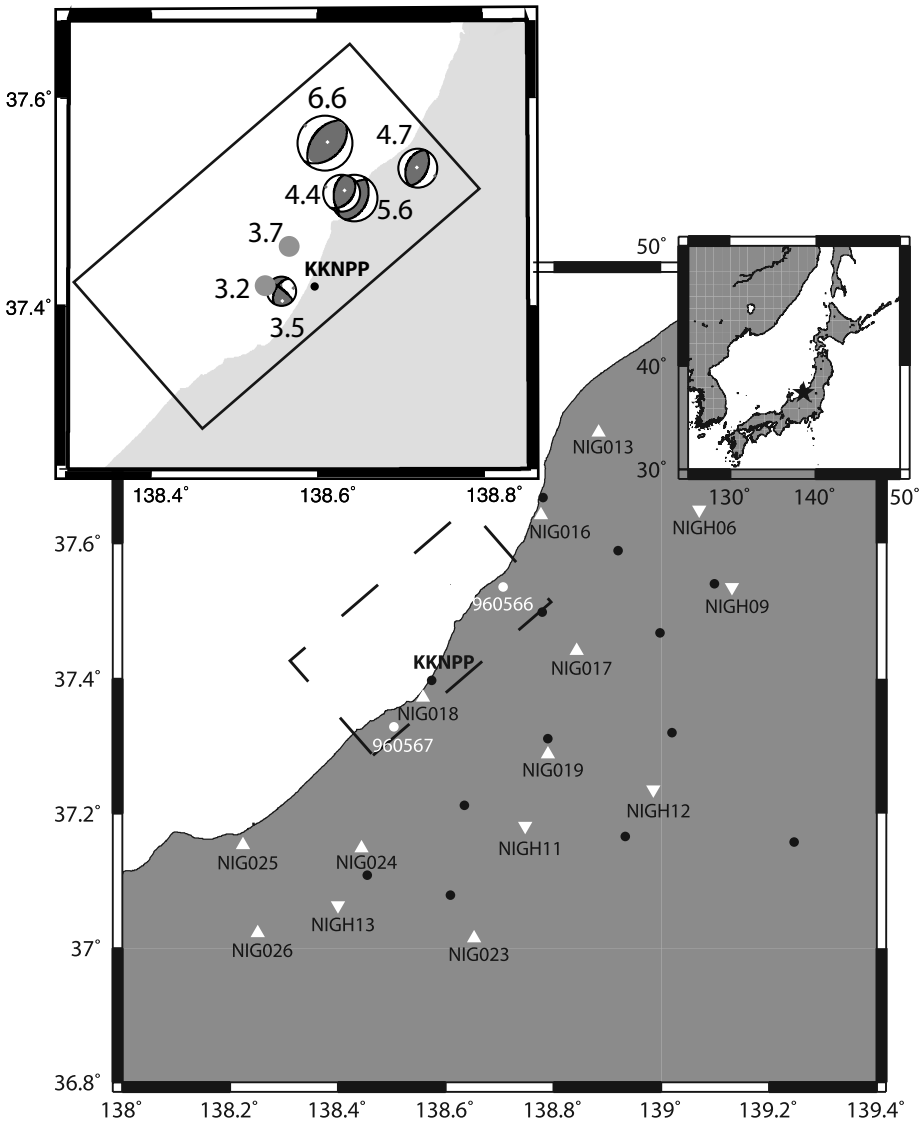
6.6
4.7
4.4
5.6
3.7
KKNPP
3.2
3.5
37.6˚
37.4˚
138.4˚
138.6˚
138.8˚
50˚
40˚
30˚
130˚
140˚
50˚
NIG013
NIG016
NIGH06
960566
NIGH09
KKNPP
NIG017
NIG018
960567
NIG019
NIGH12
NIGH11
NIG025
NIG024
NIGH13
NIG026
NIG023
37.6˚
37.4˚
37.2˚
37˚
36.8˚
138˚
138.2˚
138.4˚
138.6˚
138.8˚
139˚
139.2˚
139.4˚

Figure 1

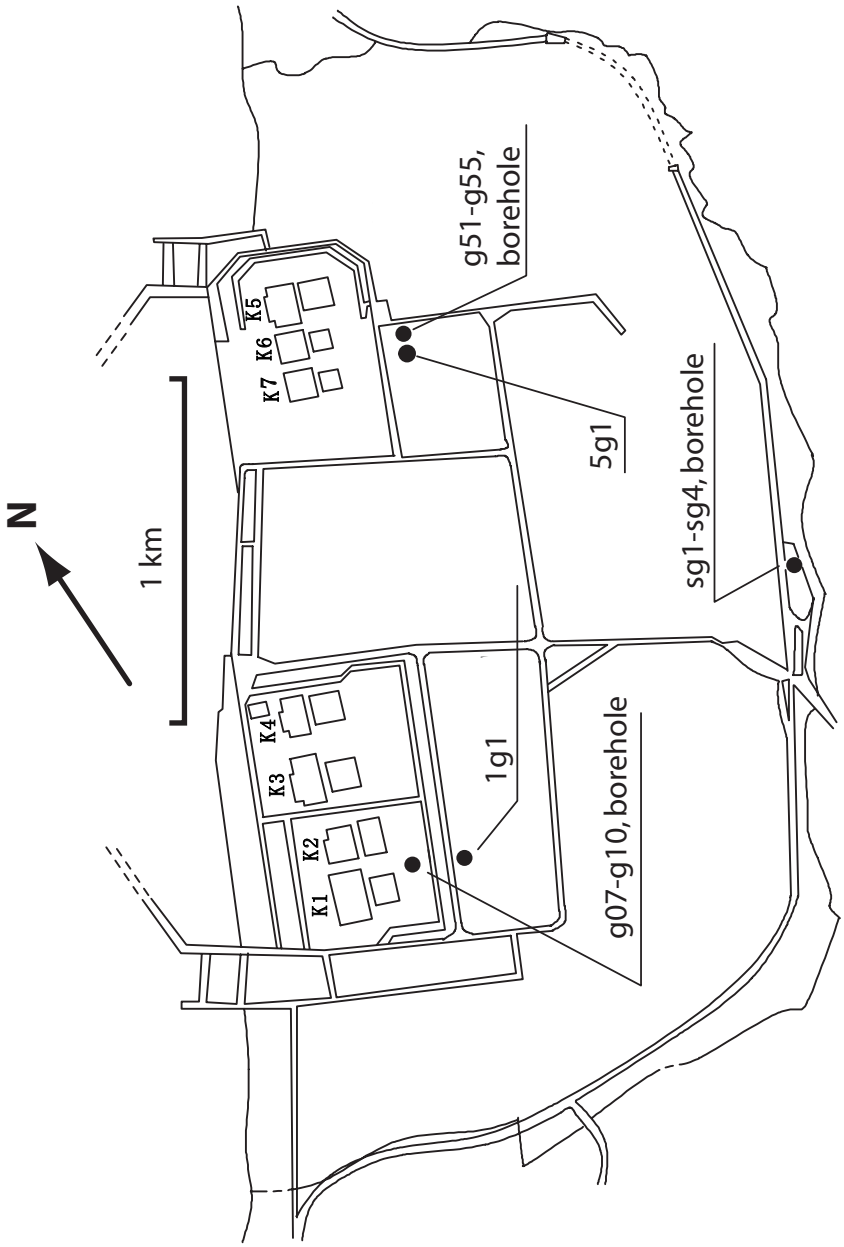
N
1 km
K1
K2
K3
K4
K5
K6
K7
1g1
5g1
g51-g55,
borehole
sg1-sg4, borehole
g07-g10, borehole

Figure 2

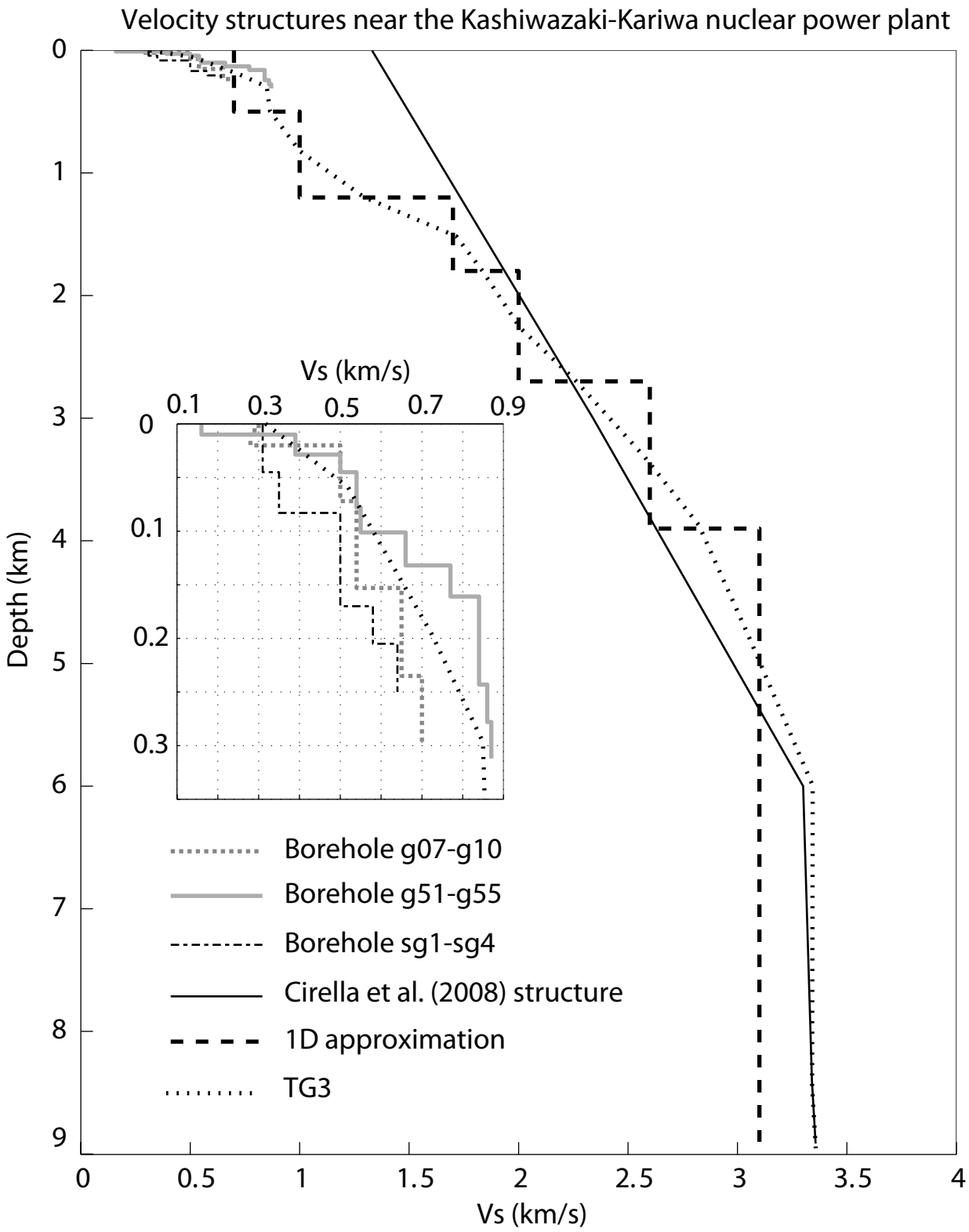
Velocity structures near the Kashiwazaki-Kariwa nuclear power plant
Depth (km)
Vs (km/s)
0
1
2
3
4
5
6
7
8
9
0
0.5
1
1.5
2
2.5
3
3.5
4
Vs (km/s)
0.1
0.3
0.5
0.7
0.9
0
0.1
0.2
0.3
Borehole g07-g10
Borehole g51-g55
Borehole sg1-sg4
Cirella et al. (2008) structure
1D approximation
TG3

Figure 3

1g1
5g1
sg1
EW
NS
UP
integrated acceleration, Gal*s
time after 2007/7/16 0112:46, s
100
50
0
25
30
35
40
45
50

Figure 4

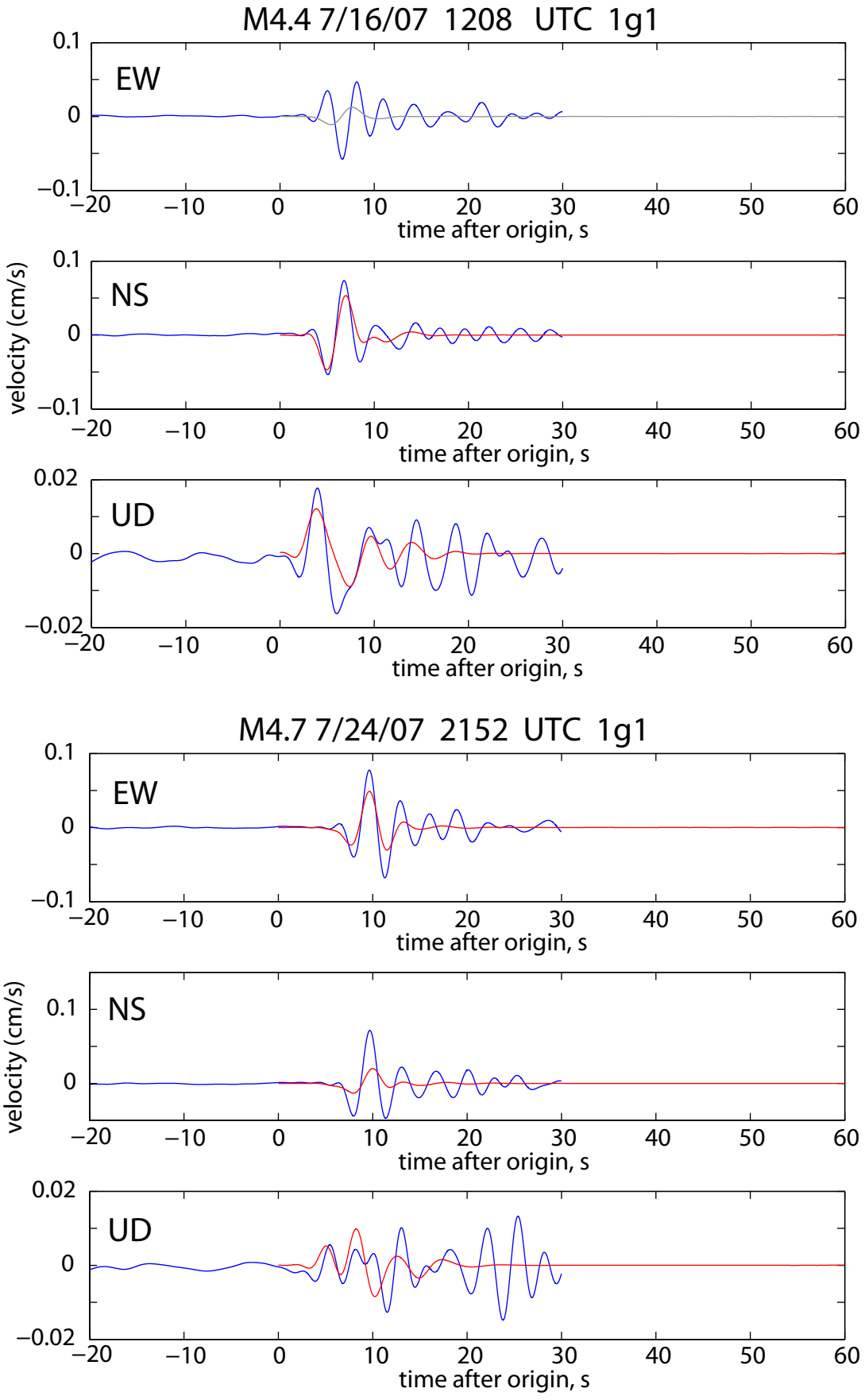
M4.4 7/16/07 1208 UTC 1g1
EW
NS
UD
velocity (cm/s)
time after origin, s
M4.7 7/24/07 2152 UTC 1g1
EW
NS
UD
velocity (cm/s)
time after origin, s

Figure 5

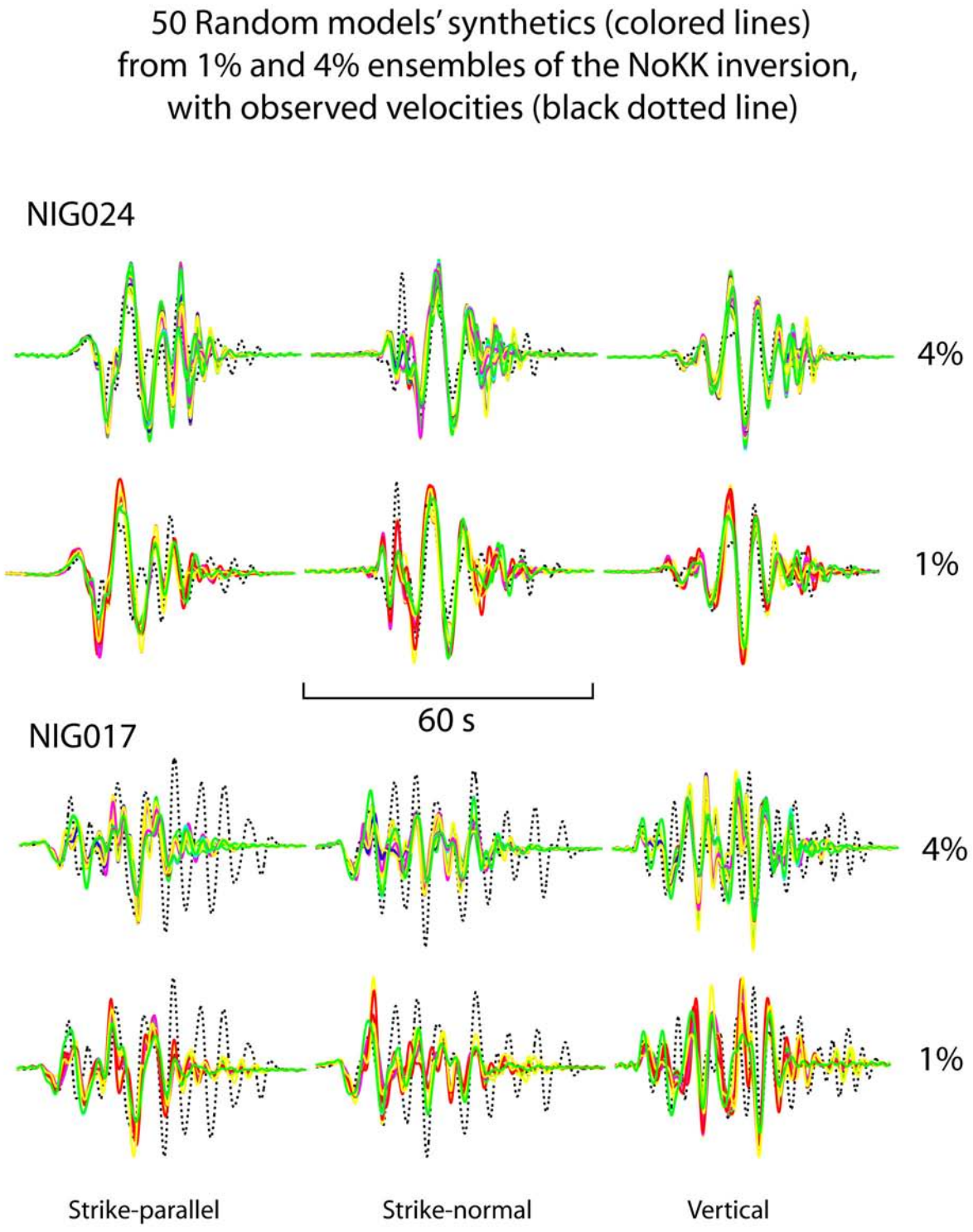
50 Random models' synthetics (colored lines)
from 1% and 4% ensembles of the NoKK inversion,
with observed velocities (black dotted line)
NIG024
4%
1%
60 s
NIG017
4%
1%
Strike-parallel
Strike-normal
Vertical

Figure 6

Velocity waveform fit, *ALL* inversion

Red = synthetic, blue = data

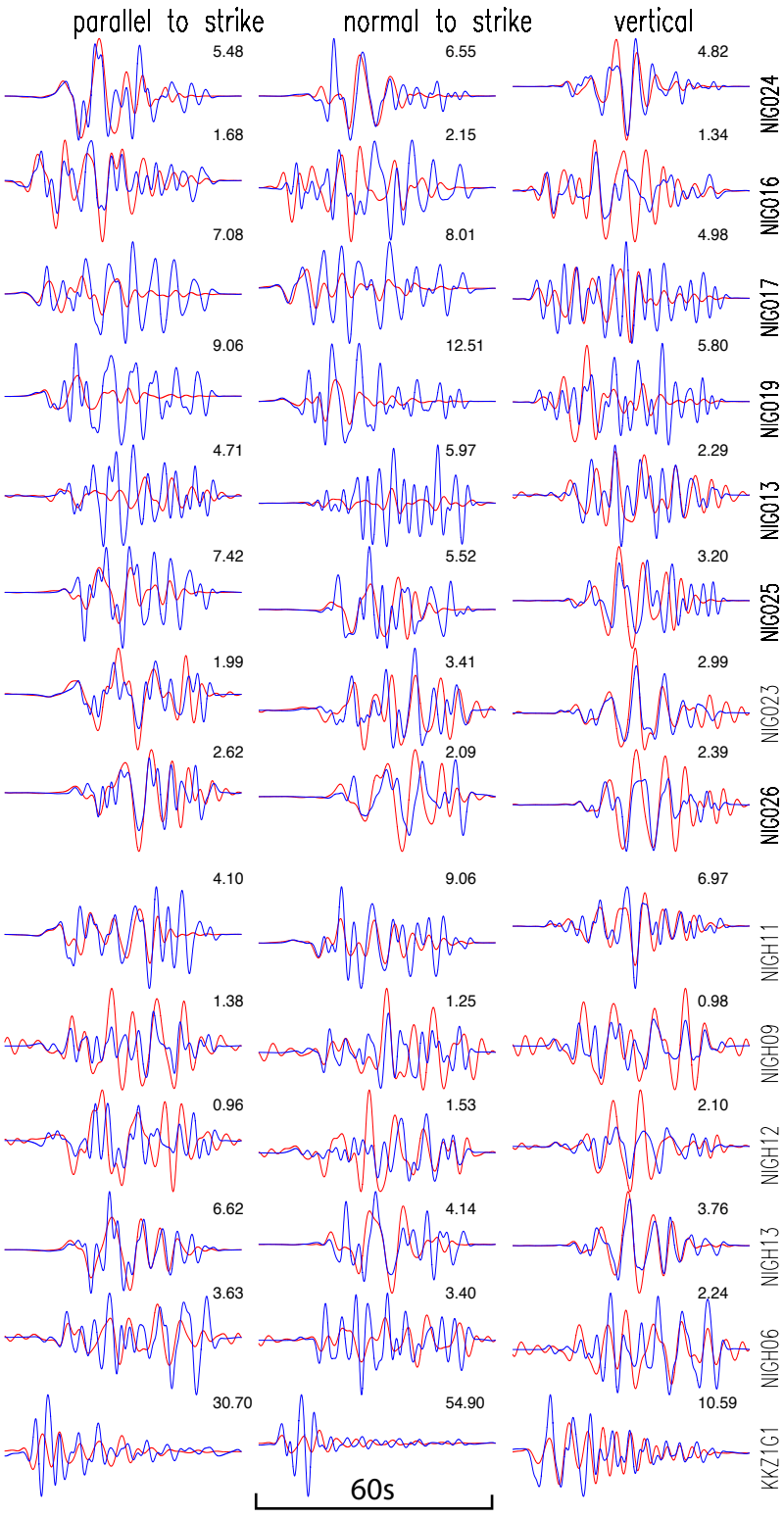

Figure 7

Velocity waveform fit, NoKK inversion

Red = synthetic, blue = data

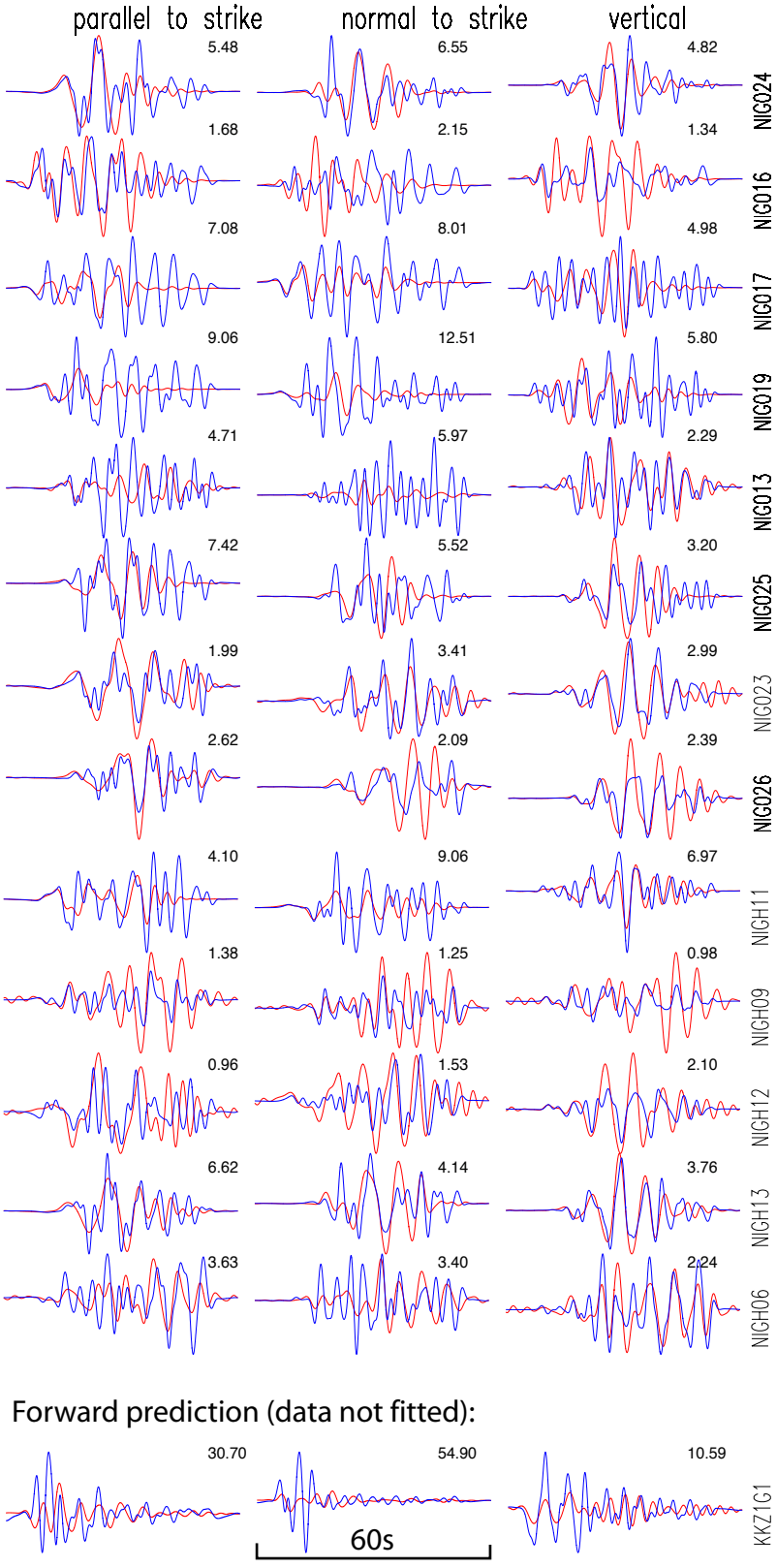

Figure 8

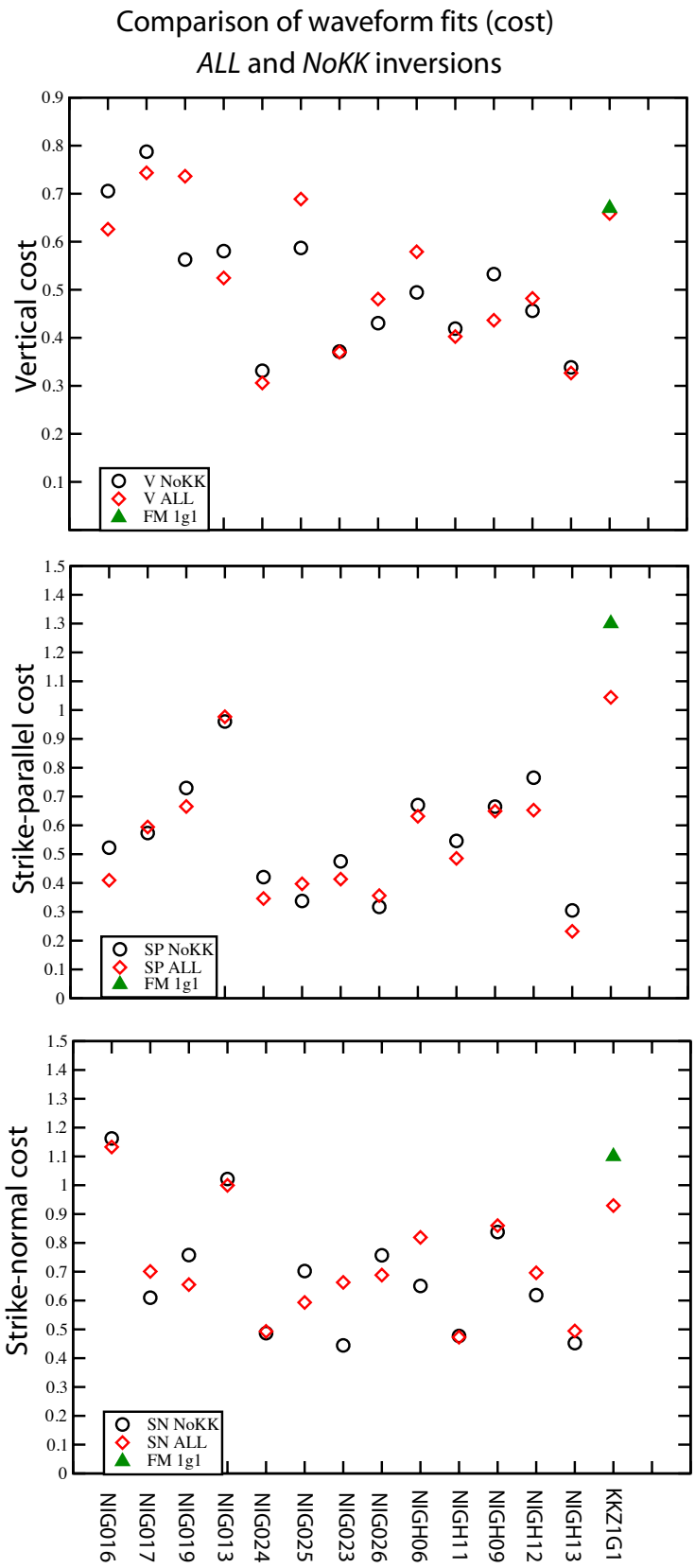
Comparison of waveform fits (cost)
ALL and NoKK inversions
Vertical cost
V NoKK
V ALL
FM 1g1
Strike-parallel cost
SP NoKK
SP ALL
FM 1g1
Strike-normal cost
SN NoKK
SN ALL
FM 1g1
NIG016
NIG017
NIG019
NIG013
NIG024
NIG025
NIG023
NIG026
NIGH06
NIGH11
NIGH09
NIGH12
NIGH13
KKZ1G1

Figure 9

Observed (1g1, 5g1) and synthetic (at 1g1) strike-parallel spectral acceleration

NoKK inversion 1% model ensemble

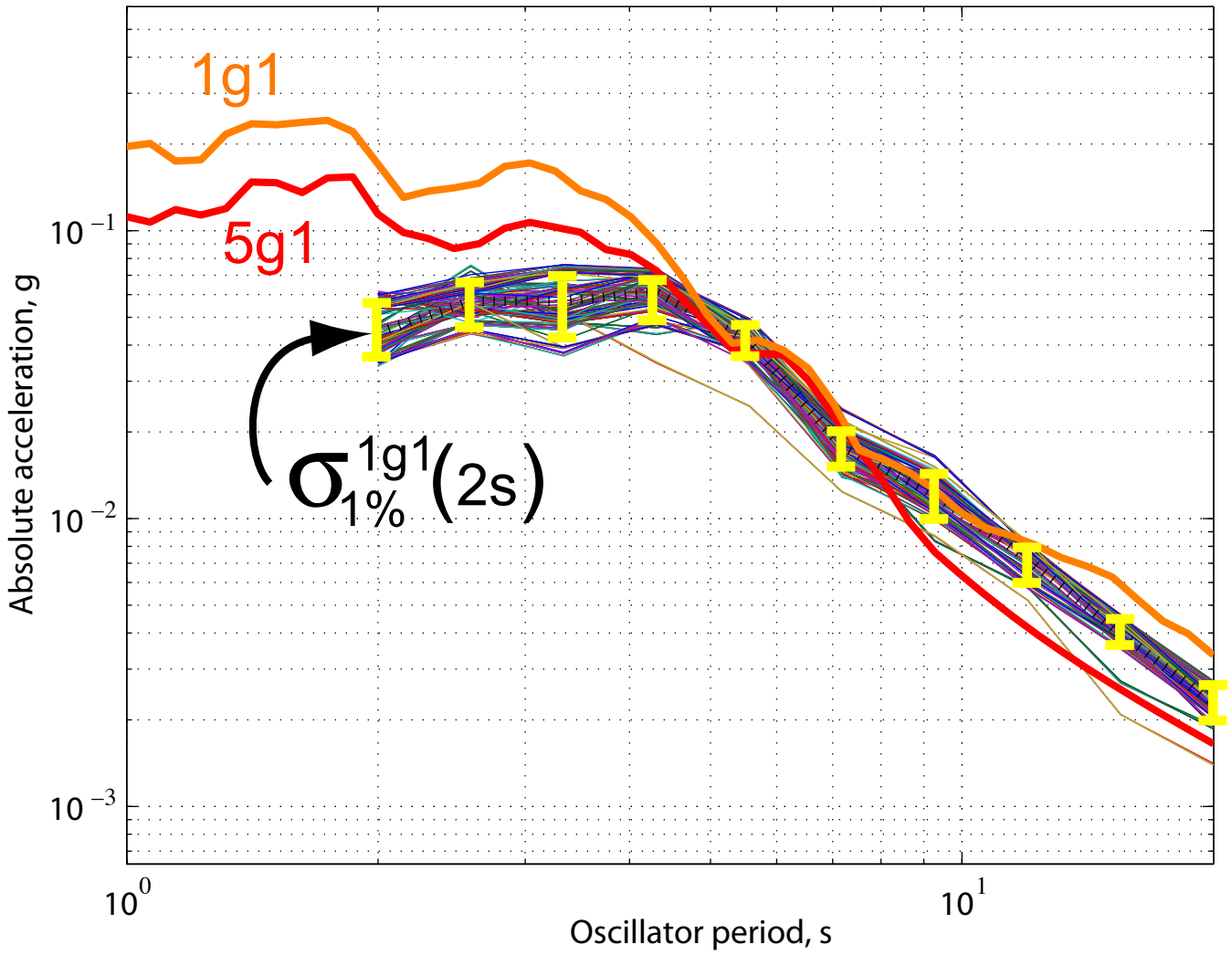

Figure 10

Biases of synthetic response spectra at station 1g1

(-) NoKK inversion, (- - - -) ALL inversion

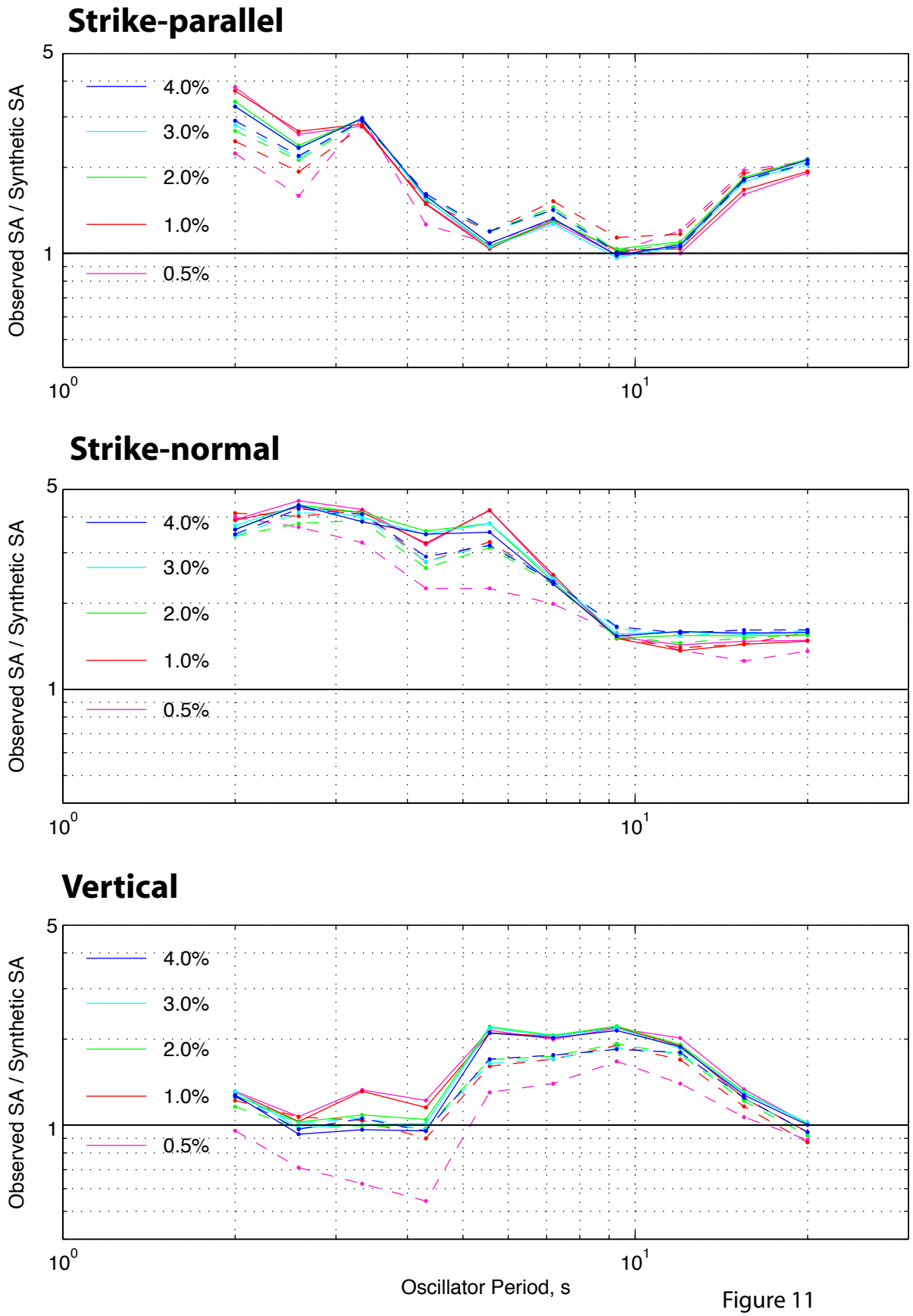

Figure 11

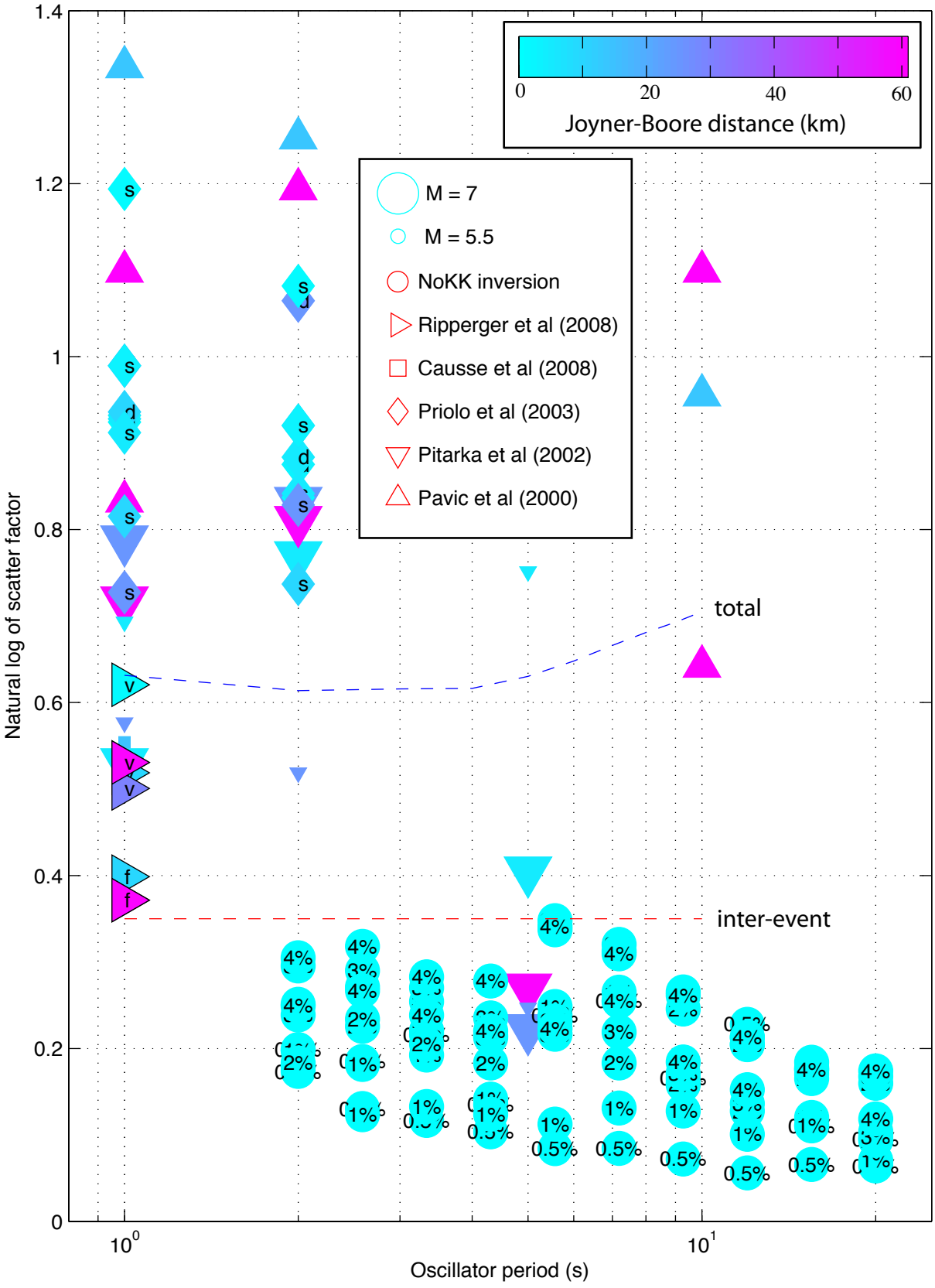
Joyner-Boore distance (km)
0
20
40
60
M = 7
M = 5.5
NoKK inversion
Ripperger et al (2008)
Causse et al (2008)
Priolo et al (2003)
Pitarka et al (2002)
Pavic et al (2000)
total
inter-event
Natural log of scatter factor
Oscillator period (s)
1.4
1.2
1
0.8
0.6
0.4
0.2
0
10^0
10^1

Figure 12

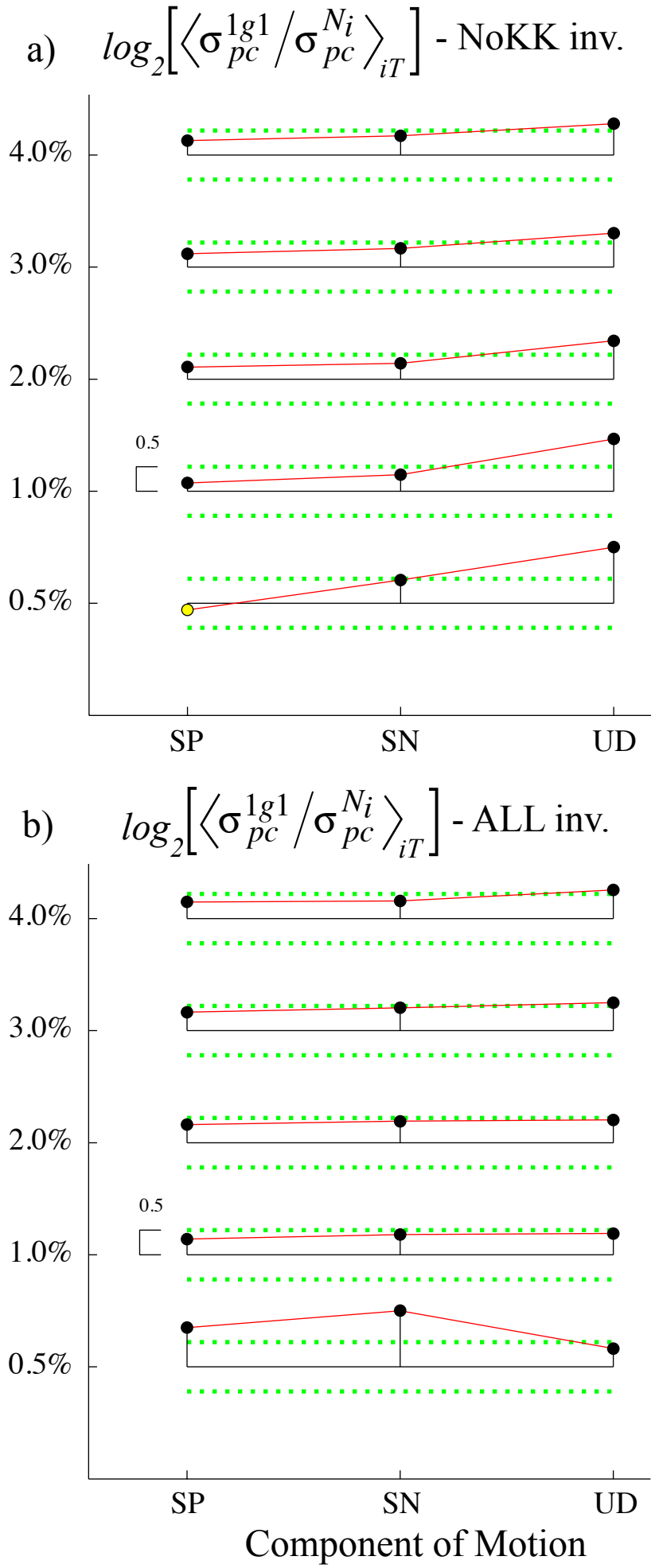
a) $log_2\left[\left\langle \sigma_{pc}^{1g1} / \sigma_{pc}^{Ni} \right\rangle_{iT}\right]$ - NoKK inv.
4.0%
3.0%
2.0%
1.0%
0.5%
0.5
SP
SN
UD
b) $log_2\left[\left\langle \sigma_{pc}^{1g1} / \sigma_{pc}^{Ni} \right\rangle_{iT}\right]$ - ALL inv.
4.0%
3.0%
2.0%
1.0%
0.5%
0.5
SP
SN
UD
Component of Motion

Figure 13

Biases of synthetic response spectra at station NIGH13

(——) Noh13 inversion, (- - - -) ALL inversion

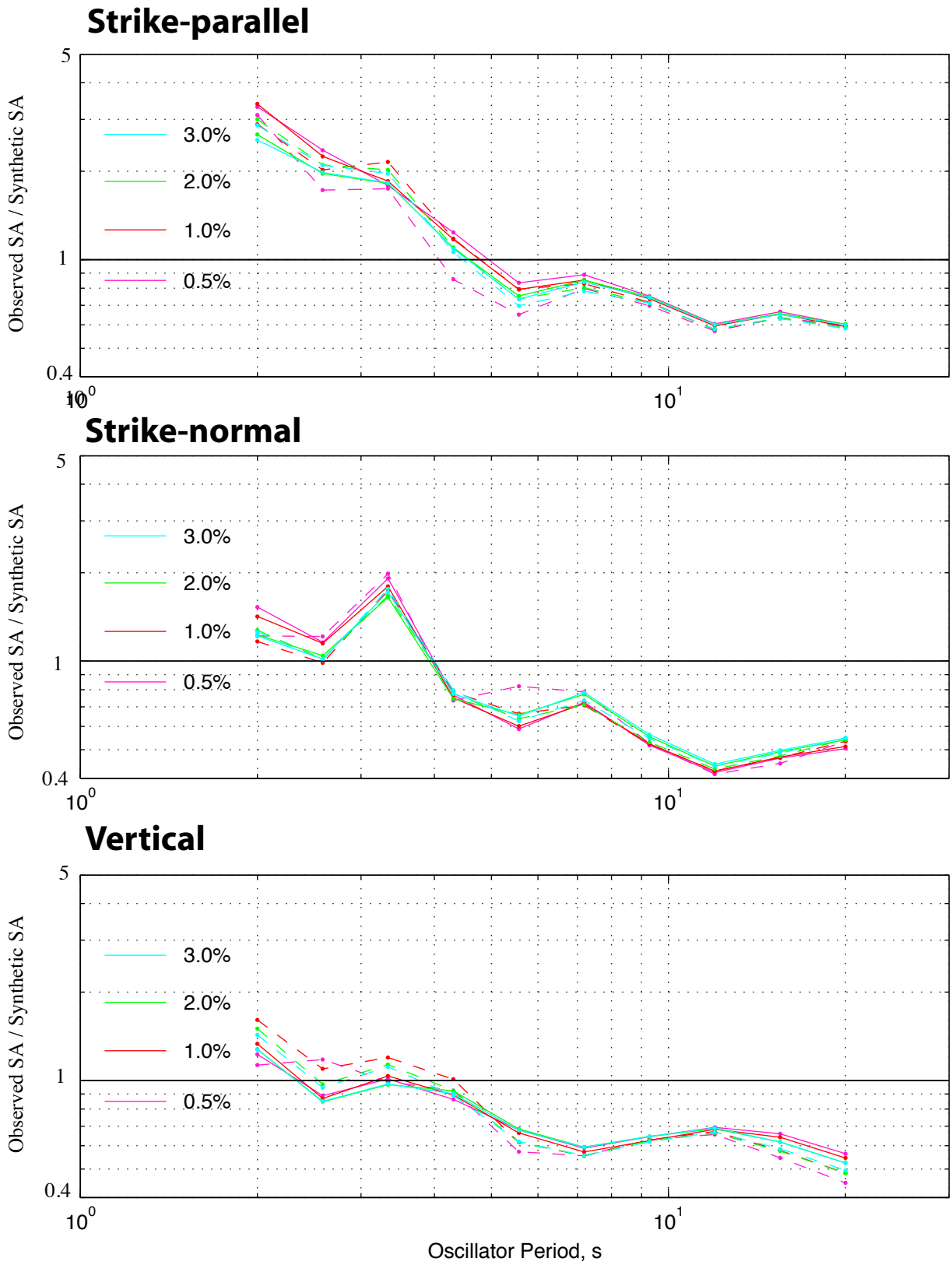

Figure 14

Velocity waveform fit, ALL inversion

Red = synthetic, blue = data

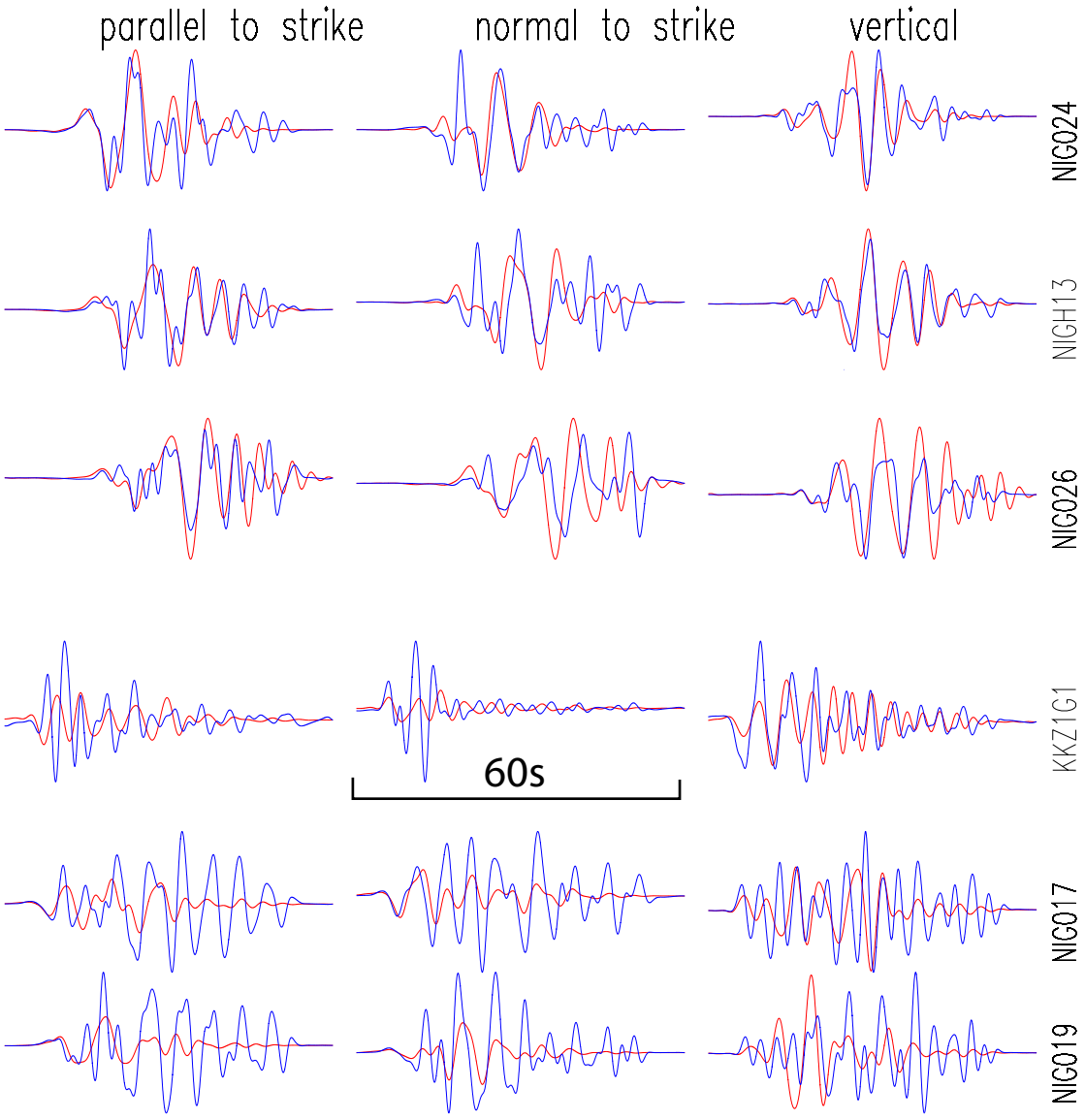

Figure 15

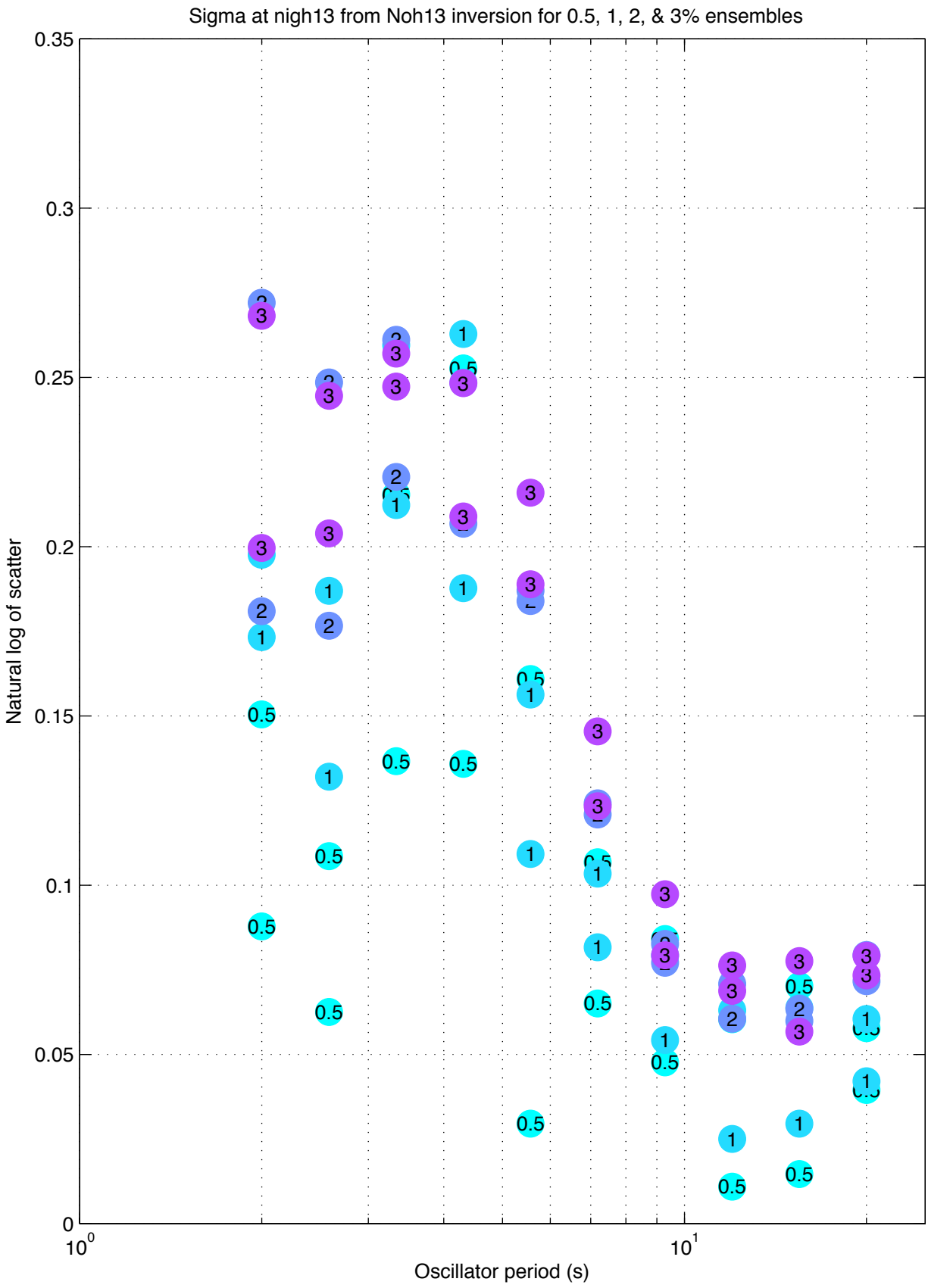
Sigma at nigh13 from Noh13 inversion for 0.5, 1, 2, & 3% ensembles
Natural log of scatter
Oscillator period (s)
0.35
0.3
0.25
0.2
0.15
0.1
0.05
0
10^0
10^1

Figure 16

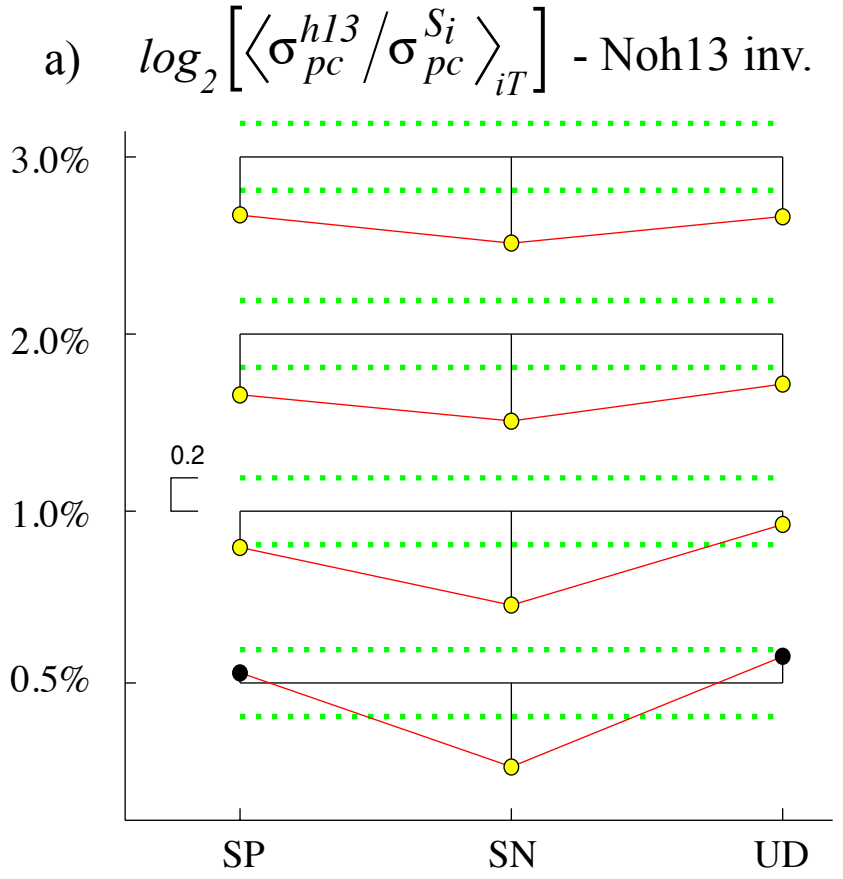
a) $log_2\left[\left\langle \sigma_{pc}^{h13} / \sigma_{pc}^{Si} \right\rangle_{iT}\right]$ - Noh13 inv.
3.0%
2.0%
1.0%
0.5%
0.2
SP
SN
UD

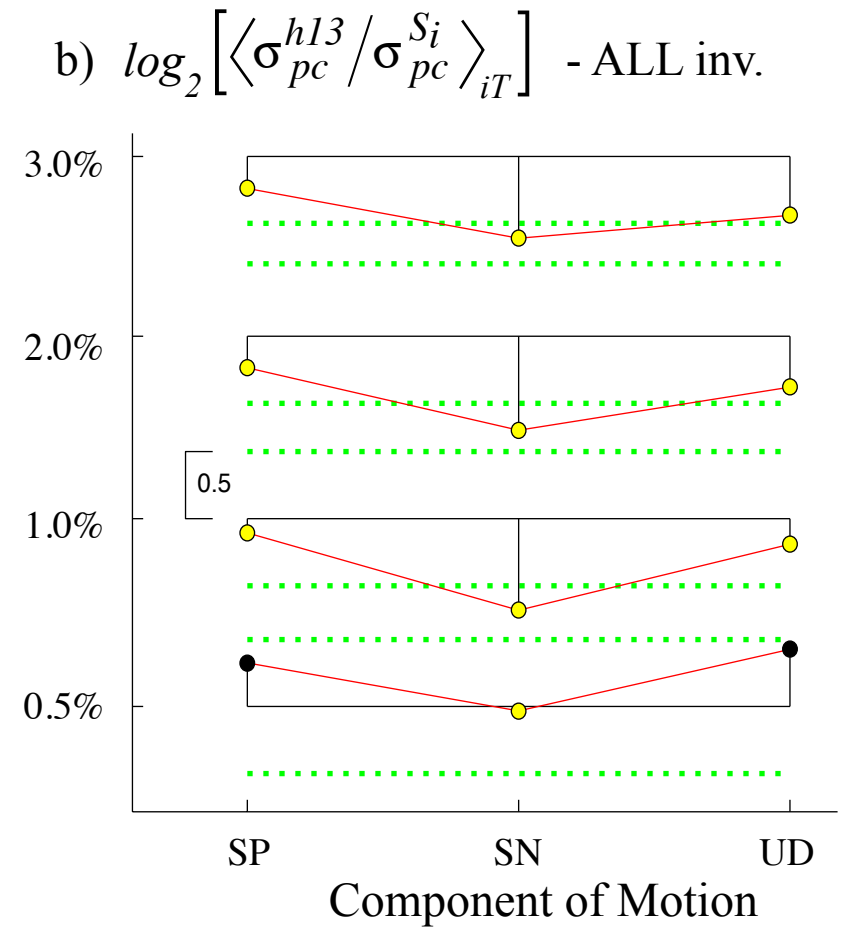
b) $log_2\left[\left\langle \sigma_{pc}^{h13} / \sigma_{pc}^{Si} \right\rangle_{iT}\right]$ - ALL inv.
3.0%
2.0%
1.0%
0.5%
0.5
SP
SN
UD
Component of Motion

Figure 17